Monthly Notices of the ROYAL ASTRONOMICAL SOCIETY

MNRAS **499,** 482–504 (2020) doi:10.1093/mnras/staa2824

An outflow powers the optical rise of the nearby, fast-evolving tidal disruption event AT2019qiz

M. Nicholl [1,2★] T. Wevers [3] S. R. Oates [1] K. D. Alexander,[4†] G. Leloudas,[5] F. Onori [6] A. Jerkstrand,[7,8] S. Gomez,[9] S. Campana,[10] I. Arcavi,[11,12] P. Charalampopoulos,[5] M. Gromadzki,[13] N. Ihanec,[13] P. G. Jonker,[14,15] A. Lawrence [2] I. Mandel [1,16,17] S. Schulze [18] P. Short [2] J. Burke,[19,20] C. McCully,[19,20] D. Hiramatsu,[19,20] D. A. Howell,[19,20] C. Pellegrino,[19,20] H. Abbot,[21] J. P. Anderson,[22] E. Berger,[9] P. K. Blanchard,[4] G. Cannizzaro [14,15] T.-W. Chen,[8] M. Dennefeld,[23] L. Galbany [24] S. González-Gaitán [25] G. Hosseinzadeh,[9] C. Inserra [26] I. Irani,[18] P. Kuin [27] T. Müller-Bravo [28] J. Pineda,[29] N. P. Ross [2] R. Roy,[30] S. J. Smartt,[31] K. W. Smith,[31] B. Tucker,[21] Ł. Wyrzykowski[13] and D. R. Young[31]

Affiliations are listed at the end of the paper

Accepted 2020 September 11. Received 2020 September 9; in original form 2020 June 3

ABSTRACT

At 66 Mpc, AT2019qiz is the closest optical tidal disruption event (TDE) to date, with a luminosity intermediate between the bulk of the population and the faint-and-fast event iPTF16fnl. Its proximity allowed a very early detection and triggering of multiwavelength and spectroscopic follow-up well before maximum light. The velocity dispersion of the host galaxy and fits to the TDE light curve indicate a black hole mass $\approx 10^6\,M_\odot$, disrupting a star of $\approx 1\,M_\odot$. By analysing our comprehensive UV, optical, and X-ray data, we show that the early optical emission is dominated by an outflow, with a luminosity evolution $L \propto t^2$, consistent with a photosphere expanding at constant velocity ($\gtrsim 2000\,\mathrm{km\,s^{-1}}$), and a line-forming region producing initially blueshifted H and He II profiles with $v = 3000$–$10\,000\,\mathrm{km\,s^{-1}}$. The fastest optical ejecta approach the velocity inferred from radio detections (modelled in a forthcoming companion paper from K. D. Alexander et al.), thus the same outflow may be responsible for both the fast optical rise and the radio emission – the first time this connection has been observed in a TDE. The light-curve rise begins 29 ± 2 d before maximum light, peaking when the photosphere reaches the radius where optical photons can escape. The photosphere then undergoes a sudden transition, first cooling at constant radius then contracting at constant temperature. At the same time, the blueshifts disappear from the spectrum and Bowen fluorescence lines (N III) become prominent, implying a source of far-UV photons, while the X-ray light curve peaks at $\approx 10^{41}\,\mathrm{erg\,s^{-1}}$. Assuming that these X-rays are from prompt accretion, the size and mass of the outflow are consistent with the reprocessing layer needed to explain the large optical to X-ray ratio in this and other optical TDEs, possibly favouring accretion-powered over collision-powered outflow models.

Key words: black hole physics – galaxies: nuclei – transients: tidal disruption events.

1 INTRODUCTION

An unfortunate star in the nucleus of a galaxy can find itself on an orbit that intersects the tidal radius of the central supermassive black hole (SMBH), where $R_\mathrm{t} \approx R_*(M_\bullet/M_*)^{1/3}$ for a black hole of mass $M_\bullet$ and a star of mass M_* and radius R_* (Hills 1975). This encounter induces a spread in the specific orbital binding energy across the star that is orders of magnitude greater than the mean binding energy (Rees 1988), sufficient to tear the star apart in a 'tidal disruption event' (TDE). The stellar debris, confined in the vertical direction by self-gravity (Kochanek 1994; Guillochon, Manukian & Ramirez-Ruiz 2014), is stretched into a long, thin stream, roughly half of which remains bound to the SMBH (Rees 1988). As the bound debris orbits the SMBH, relativistic apsidal precession causes the stream to self-intersect and dissipate energy (Dai, McKinney & Miller 2015; Shiokawa et al. 2015; Bonnerot & Lu 2020)

This destruction can power a very luminous flare, up to or exceeding the Eddington luminosity, either when the intersecting streams circularize and form an accretion disc (Rees 1988; Phinney 1989), or even earlier if comparable radiation is produced directly from the stream collisions (Piran et al. 2015; Jiang, Guillochon & Loeb 2016b). Such flares are now regularly discovered, at a rate exceeding a few per year, by the various wide-field time-domain surveys (e.g. Gezari et al. 2012; Arcavi et al. 2014; Holoien et al. 2014; van Velzen et al. 2020).

★ E-mail: mnicholl@star.sr.bham.ac.uk
† Einstein Fellow

Observed TDEs are bright in the UV, with characteristic temperatures $\sim$2–5 $\times$ 10^4 K and luminosities $\sim 10^{44}$ erg s^{-1}. They are classified according to their spectra, generally exhibiting broad, low equivalent width[1] emission lines of hydrogen, neutral and ionized helium, and Bowen fluorescence lines of doubly ionized nitrogen and oxygen (e.g. Arcavi et al. 2014; Leloudas et al. 2019). This prompted van Velzen et al. (2020) to suggest three subclasses labelled TDE-H, TDE-He, and TDE-Bowen, though some TDEs defy a consistent classification by changing their apparent spectral type as they evolve (Nicholl et al. 2019b).

TDE flares were initially predicted to be brightest in X-rays, due to the high temperature of an accretion disc, and indeed this is the wavelength where the earliest TDE candidates were identified (Komossa 2002). However, the optically discovered TDEs have proven to be surprisingly diverse in their X-ray properties. Their X-ray to optical ratios at maximum light range from $\gtrsim 10^3$ to $<10^{-3}$ (Auchettl, Guillochon & Ramirez-Ruiz 2017). Producing such luminous optical emission without significant X-ray flux can be explained in one of two ways: either X-ray faint TDEs are powered primarily by stream collisions rather than accretion, or the accretion disc emission is reprocessed through an atmosphere (Strubbe & Quataert 2009; Guillochon et al. 2014; Roth et al. 2016).

Several lines of evidence have indicated that accretion discs do form promptly even in X-ray faint TDEs: Bowen fluorescence lines that require excitation from far-UV photons (Blagorodnova et al. 2019; Leloudas et al. 2019); low-ionization iron emission appearing shortly after maximum light (Wevers et al. 2019b); and recently the direct detection of double-peaked Balmer lines that match predicted disc profiles (Hung et al. 2020; Short et al. 2020). Thus a critical question is to understand the nature and origin of the implied reprocessing layer. Guillochon et al. (2014) showed that the unbound debris stream cannot be the site of reprocessing, because its apparent cross-section is too low to intercept a significant fraction of the TDE flux.

Inhibiting progress is the messy geometry of the debris. Colliding streams, inflowing and outflowing gas, and a viewing-angle dependence on both the broad-band (Dai et al. 2018) and spectroscopic (Nicholl et al. 2019b) properties all contribute to a messy knot that must be untangled. One important clue comes from radio observations: although only a small (but growing) sample of TDEs has been detected in the radio, in such cases we can measure the properties (energy, velocity, and density) of an outflow directly (see recent review by Alexander et al. 2020). In some TDEs this emission is from a relativistic jet (Bloom et al. 2011; Burrows et al. 2011; Zauderer et al. 2011; Cenko et al. 2012; Mattila et al. 2018), which does not appear to be a common feature of TDEs, but other radio TDEs have launched subrelativistic outflows (Alexander et al. 2016, 2017; van Velzen et al. 2016; Anderson et al. 2019)

A number of radio-quiet TDEs have exhibited indirect evidence for slower outflows in the form of blueshifted optical/UV emission and absorption lines (Blanchard et al. 2017; Roth & Kasen 2018; Hung et al. 2019), suggesting that outflows may be common. This is important, as the expanding material offers a promising means to form the apparently ubiquitous reprocessing layer required by the optical/X-ray ratios. Suggested models include an Eddington envelope (Loeb & Ulmer 1997), possibly inflated by radiatively inefficient accretion or an optically thick disc wind (Metzger & Stone 2016; Dai et al. 2018), or a collision-induced outflow (Lu & Bonnerot 2020).

Understanding whether the optical reprocessing layer is connected to the non-relativistic outflows seen in some radio TDEs is therefore a crucial, and as yet under-explored, step towards a pan-chromatic picture of TDEs. Multicolour photometry at early times can reveal whether (or how quickly) the optical photosphere grows with time. Early radio detections can determine the time at which material is launched, to check for consistency with the optical flare (Alexander et al. 2016). Spectroscopy and X-ray observations can be used to search for signatures of accretion. In principle this could allow us to distinguish whether outflows are launched *by* accretion, or *before* accretion (i.e. in the collisions that ultimately enable disc formation).

In this paper, we present a detailed study of the UV, optical and X-ray emission from AT2019qiz: the closest TDE discovered to date, and the first optical TDE at $z < 0.02$ that has been detected in the radio. We place a particular focus on the spectroscopic evolution, finding clear evidence of an outflow launched well before the light curve maximum. By studying the evolution of the photosphere and line velocities, we infer a roughly homologous structure, with the fastest optically emitting material (the reprocessing layer) likely also responsible for the radio emission (which is analysed in detail in a forthcoming companion paper; Alexander et al., in preparation). This event suggests a closer connection between the optical and radio TDE outflows than has been appreciated to date, while a peak in the X-ray light curve and the detection of Bowen lines indicates that accretion began promptly in this event and likely drives the outflow. The rapid rise and decline of the light curve suggests that the properties of outflows may be key to understanding the fastest TDEs.

We detail the discovery and classification of AT2019qiz in Section 2, and describe our observations and data reduction in Section 3. We analyse the host galaxy, including evidence for a pre-existing AGN, in Section 4, and study the photometric and spectroscopic evolution of the TDE emission in Sections 5 and 6. This is then brought together into a coherent picture, discussed in Section 7, before we conclude in Section 8. All data in this paper will be made publicly available via WISeREP (Yaron & Gal-Yam 2012).

2 DISCOVERY AND BACKGROUND

AT2019qiz was discovered in real-time alerts from the Zwicky Transient Facility (ZTF; Bellm et al. 2019; Masci et al. 2019; Patterson et al. 2019), at coordinates RA = 04:46:37.88, Dec. = −10:13:34.90, and was given the survey designation ZTF19abzrhgq. It is coincident with the centre of the galaxy 2MASX J04463790-1013349 (a.k.a. WISEA J044637.88-101334.9). The transient was first identified by the ALeRCE broker, who reported it to the Transient Name Server on 2019-09-19 UT (Forster 2019). It was also reported by the AMPEL broker a few d later. In subsequent nights the same transient was independently reported by the Asteroid Terrestrial impact Last Alert System (ATLAS; Tonry et al. 2018) as ATLAS19vfr, by *Gaia* Science Alerts (Hodgkin et al. 2013) as Gaia19eks, and by the Panoramic Survey Telescope And Rapid Response System (PanSTARRS) Survey for Transients (PSST; Huber et al. 2015) as PS19gdd. The earliest detection is from ATLAS on 2019-09-18 UT.

We have been running the Classification Survey for Nuclear Transients with Liverpool and Lasair (C-SNAILS; Nicholl et al. 2019a) to search for TDEs in the public ZTF alert stream. AT2019qiz passed our selection criteria (based on brightness and proximity to the centre of the host galaxy[2]) on 2019-09-25 UT, and we

[1]Compared to other nuclear transients such as active galactic nuclei

[2]The source could have been triggered 5 d earlier but for missing offset information in the alert packet.

triggered spectroscopy with the Liverpool Telescope. On the same day, Siebert et al. (2019) publicly classified AT2019qiz as a TDE using spectroscopy from Keck I.

Their reported spectrum, and our own data obtained over the following nights, showed broad He II and Balmer emission lines superposed on a very blue continuum, characteristic of UV–optical TDEs. Follow-up observations from other groups showed that the source was rising in the UV (Zhang et al. 2019), but was not initially detected in X-rays (Auchettl et al. 2019). Radio observations with the Australia Telescope Compact Array (ATCA) revealed rising radio emission, reaching 2.6 mJy at 21.2 GHz on 2019-12-02 (O'Brien et al. 2019), placing AT2019qiz among the handful of TDEs detected at radio wavelengths.

The spectroscopic redshift of AT2019qiz, as listed for the host galaxy in the NASA Extragalactic Database (NED) and measured from narrow absorption lines in the TDE spectrum, is $z = 0.01513$. This corresponds to a distance of 65.6 Mpc, assuming a flat cosmology with $H_0 = 70\,\mathrm{km\,s^{-1}\,Mpc^{-1}}$ and $\Omega_\Lambda = 0.7$. This makes AT2019qiz the most nearby TDE discovered to date.

AT2019qiz was included in the sample of 17 TDEs from ZTF studied by van Velzen et al. (2020). Their work focused primarily on the photometric evolution around peak, and correlations between TDE and host galaxy properties. In this paper, we analyse a rich data set for AT2019qiz including densely sampled spectroscopy, very early and late photometric observations, and the first detection of the source in X-rays. We also examine the host galaxy in detail. While we link the optical properties of the TDE to its behaviour in the radio, the full radio data set and analysis will be presented in a companion paper (Alexander et al., in preparation).

3 OBSERVATIONS

3.1 Ground-based imaging

Well-sampled host-subtracted light curves of AT2019qiz were obtained by the ZTF public survey, in the *g* and *r* bands, and ATLAS in the *c* and *o* bands (effective wavelengths 5330 and 6790 Å). The ZTF light curves were accessed using the Lasair alert broker[3] (Smith et al. 2019).

We triggered additional imaging with a typical cadence of 4 d in the *g*, *r*, *i* bands using the Las Cumbres Observatory (LCO) global network of 1-m telescopes (Brown et al. 2013). We retrieved the reduced (de-biased and flat-fielded) images from LCO and carried out point spread function (PSF) fitting photometry using a custom wrapper for DAOPHOT. The zero-point in each image was calculated by comparing the instrumental magnitudes of field stars with their catalogued magnitudes from PanSTARRS data release 1 (Flewelling et al. 2016).

AT2019qiz resides in a bright galaxy, 2MASX J04463790-1013349, with $mr = 14.2$ mag (Section 4). A three-colour (*gri*) image of the host, comprised of deep stacks from PanSTARRS, is shown in Fig. 1. To isolate the transient flux, we aligned each LCO image with the PanSTARRS image in the corresponding filter using the GEOMAP and GEOTRAN tasks in PYRAF, computing the transformation from typically >50 stars, before convolving the PanSTARRS reference image to match the PSF of the science image and subtracting with HOTPANTS (Becker 2015).

[3]https://lasair.roe.ac.uk

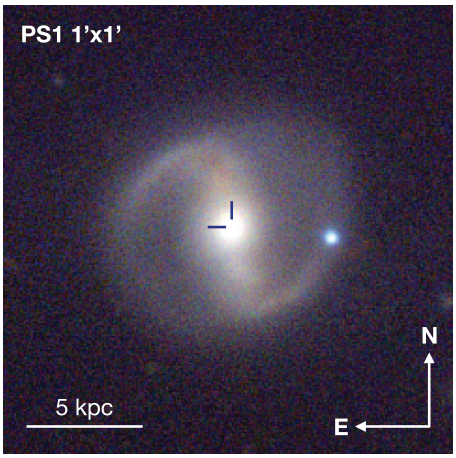

Figure 1. Pre-disruption *g*, *i*, *z* colour image of the host of AT2019qiz, 2MASX J04463790−1013349, obtained from the PanSTARRS image server. Comparing to our highest S/N LCO image of the transient, we measure an offset of 15 ± 46 pc from the centre of the host.

3.2 Astrometry

Measuring the TDE position in an LCO *r* band image obtained on 2019-10-10 (at the peak of the optical light curve), and the centroid of the galaxy in the aligned PanSTARRS *r* band image, we measure an offset of 0.12 ± 0.37 pixels (or 0.047 ± 0.144 arcsec) between the transient and the host nucleus, where the uncertainty is dominated by the root-mean-square error in aligning the images. This corresponds to a physical offset of 15 ± 46 pc at this distance; the transient is therefore fully consistent with a nuclear origin.

An alternative astrometric constraint can be obtained using the *Gaia* Science Alerts (GSA) detections (Hodgkin et al. 2013). Gaia19eks was discovered at a separation of 38 milliarcseconds (mas) from the reported location of its host galaxy in *Gaia* data release 2 (GDR2; Gaia Collaboration 2018). The estimated astrometric uncertainty of GSA is ∼100 mas (Fabricius et al. 2016), and the coordinate systems of GSA and GDR2 are well aligned (Kostrzewa-Rutkowska et al. 2018; Wevers et al. 2019b). This measurement corresponds to an even tighter constraint on the offset of 12 ± 32 pc.

3.3 *Swift* UVOT data

Target-of-opportunity observations spanning 39 epochs (PIs Yu and Nicholl) were obtained with the UV-Optical Telescope (UVOT) and X-ray Telescope (XRT) onboard the Neil Gehrels Swift Observatory (*Swift*). The UVOT light curves were measured using a 5 arcsec aperture. This is approximately twice the UVOT point-spread function, ensuring the measured magnitudes capture most of the transient flux while minimizing the host contribution (the coincidence loss correction for the UVOT data is also determined using a 5 arcsec aperture, ensuring a reliable calibration of these magnitudes). The count rates were obtained using the *Swift* UVOTSOURCE tools and converted to magnitudes using the UVOT photometric zero-points (Breeveld et al. 2011). The analysis pipeline used software HEADAS 6.24 and UVOT calibration 20170922. We exclude the initial images in the *B*, *U*, *UVW*1, and *UVW*2 filters (OBSID 00012012001) due to trailing within the images. We also exclude 2 later *UVW*1 images and a *UVW*2 image due to the source being located on patches of the

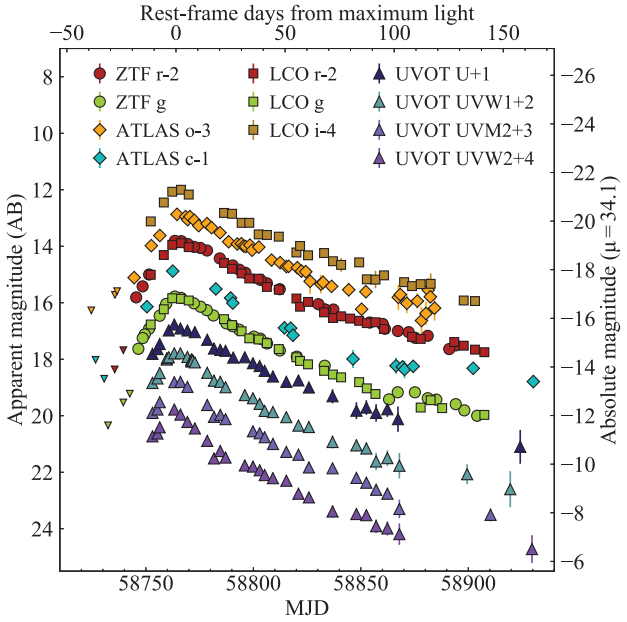

Figure 2. Optical and UV light curves of AT2019qiz. The host contribution has been removed using image differencing (ZTF, ATLAS, LCO) or subtraction of fluxes estimated from the galaxy SED (UVOT).

detector known to suffer reduced sensitivity. A correction has yet to be determined for these patches.[4]

No host galaxy images in the UV are available for subtraction. We estimated the host contribution using a spectral energy distribution (SED) fit to archival data for this galaxy (details in Section 4). The host magnitude and its error in each UVOT band was estimated using the mean and standard deviation of SED samples drawn from the posterior of this fit. We then scaled the predicted flux by a factor 0.2, i.e. the fraction of the host light within a 5 arcsec aperture in the PanSTARRS *g*-band image of the galaxy, before subtracting from the transient photometry. We checked that this method provides a reliable correction for the host flux by re-extracting the UVOT light curve using a 30 arcsec aperture to fully capture both the transient and host flux, and subtracting the model host magnitudes with no scaling.

Comparing the 5 arcsec light curves to the 30 arcsec light curves, we find a good match in the *U* and *UVW*1 bands. In the bluer *UVM*2 and *UVW*2 bands, where the host SED and light profile is less constrained, we find that scaling the host flux by a factor 0.1 before subtraction yields better agreement, and we adopt this as our final light curve. The fractional uncertainty ($\approx$ 20 per cent) in the host flux was combined in quadrature with that of the transient flux when calculating the photometric errors. We show in Appendix A a comparison between the UVOT light curves obtained using the 5 and 30 arcsec apertures. The complete, host-subtracted UV and optical light curves from *Swift*, LCO, ZTF and ATLAS are shown in Fig. 2.

3.4 *Swift* XRT data

We processed the XRT data using the online analysis tools provided by the UK *Swift* Science Data Centre (Evans et al. 2007, 2009). We first combined all of the data into a single deep stack (total exposure time 30 ks), which we then downloaded for local analysis. The stacked image, shown in Fig. 3, clearly exhibits an X-ray source at the position of AT2019qiz. Using a 50 arcsec aperture (∼2.5 times the instrumental half-energy width) centred at the coordinates of the transient, we measure an excess 46.9 ± 8.4 counts above the background, giving a mean count rate of $(1.6 \pm 0.3) \times 10^{-3}$ ct s^{-1}.

[4] https://heasarc.gsfc.nasa.gov/docs/heasarc/caldb/swift/docs/uvot/uvotcaldb_sss_01.pdf

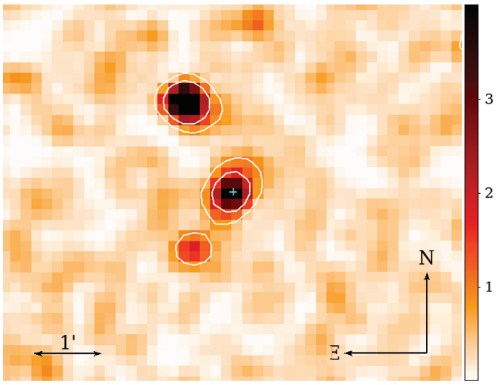

Figure 3. Stacked *Swift* XRT image (total exposure time 30 ks) centred at the position of AT2019qiz, marked by a cyan cross. An X-ray source is detected at 5.6σ significance. The image has been blocked 4 × 4 and smoothed using a Gaussian kernel for display. The colour bar gives the counts per pixel.

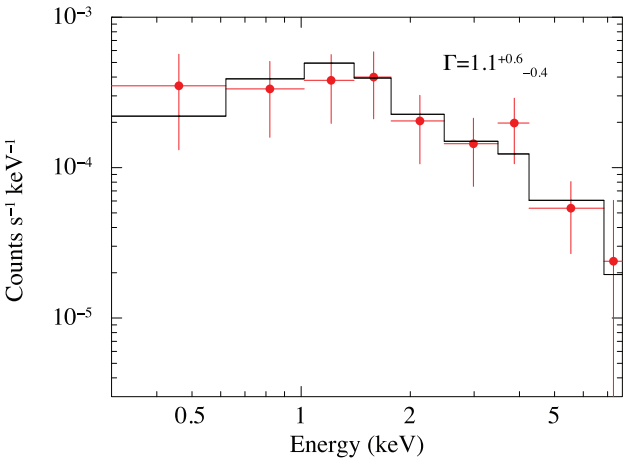

Figure 4. Time-averaged X-ray spectrum and best-fitting absorbed power-law model, used to derive the counts-to-flux conversion.

We then used the same tools to extract the mean X-ray spectrum, shown in Fig. 4, and light curve. Given the low number of counts we fit the spectrum using Cash statistics, and fixed the Galactic column density to 6.5×10^{20} cm^{-2}. The fit with a power law does not need an intrinsic column ($<2.8 \times 10^{21}$ cm^{-2}, 90 per cent confidence level). The photon index of the fit is $\Gamma = 1.1^{+0.6}_{-0.4}$. A blackbody model can give a comparable fit, but the inferred temperature and radius ($kT = 0.9$ keV, $R = 6.0 \times 10^7$ cm) are not consistent with other TDEs. Such a radius is also much smaller than the Schwarzschild radius of a SMBH, however an apparently small emitting surface can also arise due to obscuration (Wevers et al. 2019a). The 0.3–10 keV unabsorbed flux from the power-law fit is $9.9^{+3.7}_{-3.4} \times 10^{-14}$ er g cm^{-2} s^{-1}. At the distance of AT2019qiz, this corresponds to an X-ray luminosity $L_X = 5.1 \times 10^{40}$ erg s^{-1}.

The X-ray light curve is shown in Fig. 5. We specify a target bin size of 10 counts above background, with a minimum of three counts to form a bin. The 0.3–10 keV light curve peaks around 25 d

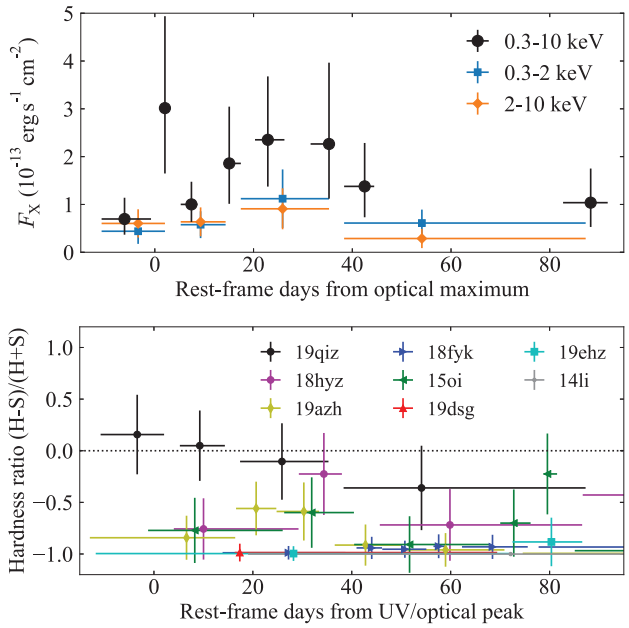

Figure 5. Top: XRT light curve (unabsorbed flux) in 0.3–10 keV, 0.3–2 keV (soft), and 2–10 keV (hard) X-ray bands. The X-ray light curve peaks around 25 d after optical maximum. Bottom: evolution of the hardness ratio, defined as (hard − soft counts)/(hard + soft counts). The X-rays transition from hard to soft as the luminosity declines. This is in contrast to most X-ray TDEs that exhibit at all times a soft spectrum (Holoien et al. 2016a,b; Gomez et al. 2020; van Velzen et al. 2020).

after optical maximum. We calculate the evolution of the hardness ratio as $(H - S)/(H + S)$, where S is the count rate in the 0.3–2 keV band and H the count rate in the 2–10 keV band; these ranges have been chosen to match Auchettl et al. (2017). The pipeline necessarily returns coarser temporal bins for the hardness ratio, due to the lower counts when dividing into the two bands. We compare this ratio to other TDEs with well-sampled XRT detections. AT2019qiz exhibits an unusually hard ratio at early times, with $(H - S)/(H + S) = 0.2 \pm 0.3$, but as the X-rays fade they also soften, reaching $(H - S)/(H + S) = -0.4 \pm 0.3$ by ≈50 d after peak. This latter value is typical of the TDE sample studied by Auchettl et al. (2017), whereas a positive ratio has only been seen previously in the jetted TDE J1644+57 (Zauderer et al. 2011).

3.5 Optical spectroscopic data

Spectra of AT2019qiz were obtained from the 3.6-m New Technology Telescope (NTT), using EFOSC2 with Grism#11, through the advanced Public ESO Spectroscopy Survey of Transient Objects (ePESSTO+; Smartt et al. 2015); the LCO 2-m North and South telescopes with FLOYDS; the 2-m Liverpool Telescope (LT) with SPRAT (Piascik et al. 2014) in the blue-optimized setting, as part of C-SNAILS (Nicholl et al. 2019a); the 6.5-m MMT telescope with Binospec (Fabricant et al. 2019); the 6.5-m Magellan Clay telescope with LDSS-3 and the VPH-ALL grism; the 4.2-m William Herschel Telescope with ISIS (Jorden 1990) and the R600 blue/red gratings; and the 8-m ESO Very Large Telescope using X-Shooter (Vernet et al. 2011) in on-slit nodding mode, through our TDE target-of-opportunity program.

Reduction and extraction of these data were performed using instrument-specific pipelines or (in the cases of the LDSS-3 and ISIS data) standard routines in IRAF. Reduced LCO and LT data were downloaded from the respective data archives, while we ran the pipelines (Freudling et al. 2013; Smartt et al. 2015) locally for the EFOSC2 and X-Shooter data.[5] Typical reduction steps are de-biasing, flat-fielding and wavelength-calibration using standard lamps, cosmic-ray removal (van Dokkum, Bloom & Tewes 2012), flux calibration using spectra of standard stars obtained with the same instrument set-ups, and variance-weighted extraction to a one-dimensional spectrum. We also retrieved the reduced classification spectrum obtained by Siebert et al. (2019) using the 10-m Keck-I telescope with LRIS (Oke et al. 1995), and made public via the Transient Name Server.[6] All spectra are corrected for redshift and a foreground extinction of $E(B - V) = 0.0939$ using the dust maps of Schlafly & Finkbeiner (2011) and the extinction curve from Cardelli, Clayton & Mathis (1989). All spectra are plotted in Fig. 6. For host-subtracted spectra (Section 4 and Appendix A), we apply these corrections after scaling and subtraction.

4 HOST GALAXY PROPERTIES

4.1 Morphology

The host of AT2019qiz is a face-on spiral galaxy. A large-scale bar is visible in the PanSTARRS image (Fig. 1). French et al. (2020b) analysed *Hubble Space Telescope* (*HST*) images of four TDE hosts and identified bars in two. While central bars (on scales $\lesssim 100$ pc) can increase the TDE rate by dynamically feeding stars towards the nucleus (Merritt & Poon 2004), there is no evidence that large-scale bars increase the TDE rate (French et al. 2020b). Given the proximity of AT2019qiz, this galaxy is an ideal candidate for *HST* or adaptive optics imaging to resolve the structure of the nucleus.

Recent studies have shown that TDE host galaxies typically have a more central concentration of mass than the background galaxy population (Law-Smith et al. 2017; Graur et al. 2018). The most recent compilation (French et al. 2020a) shows that the Sérsic indices of TDE hosts range from ≈1.5–6, consistent with the background distribution of quiescent galaxies but significantly higher than star-forming galaxies. We measure the Sérsic index for the host of AT2019qiz by fitting the light distribution in the PanSTARRS *r*-band image in a 200 × 400 pixel box, centred on the nucleus, using GALFIT (Peng et al. 2002). The residuals are shown in Fig. 7. We do not fit for the spiral structure. Following French et al. (2020b), we investigate the effect of including an additional central point source (using the point-spread function derived from stars in the image as in Section 3.1). The residuals appear flatter when including the point source, however the change in reduced χ^2 is minor ($\chi^2 = 1.36$ with the point source or 1.46 without). The best-fit Sérsic index is 5.2 (with the point source) or 6.3 (without). In either case, this is consistent with the upper end of the observed distribution for TDE hosts.

4.2 Velocity dispersion and black hole mass

Following Wevers et al. (2017, 2019a), we fit the velocity dispersion of stellar absorption lines with the code PPXF (Cappellari 2017) to estimate the mass of the central SMBH. We use a late-time spectrum obtained from X-shooter, resampled to a logarithmic spacing in wavelength and with the continuum removed via polynomial fits. We find a dispersion $\sigma = 69.7 \pm 2.3$ km s^{-1}.

[5]The atmospheric dispersion corrector on X-Shooter failed on 2019-10-10, so we were unable to reduce the data in the UVB arm for this epoch.
[6]https://wis-tns.weizmann.ac.il

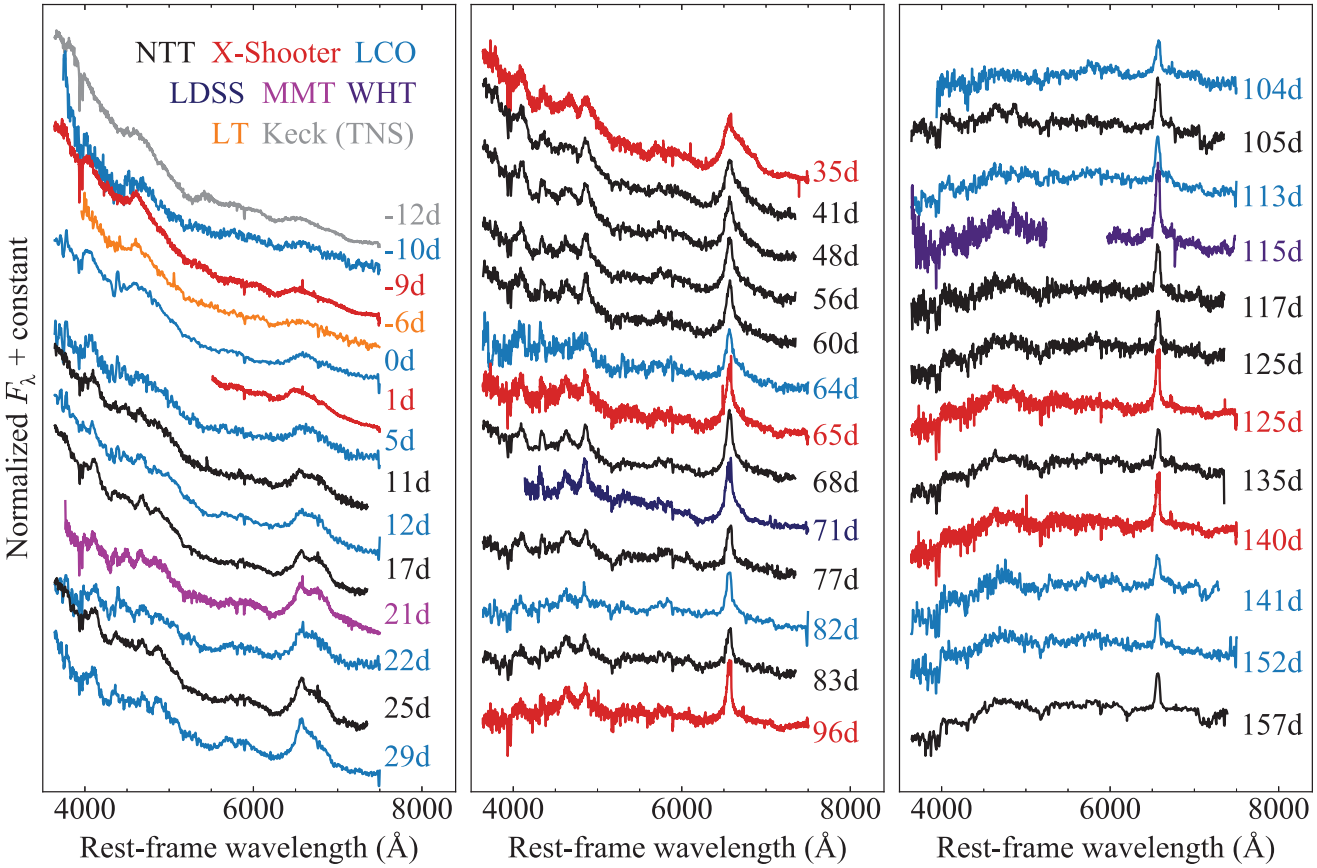

Figure 6. Complete series of spectra of AT2019qiz at phases from 12 d before until 157 d after the UV/optical peak. The phase of each spectrum is labelled, while colours individuate the telescopes/instruments used for the observations. The continuum transitions from TDE- to host-dominated over time, but broad TDE emission lines are visible throughout. A version of this figure with host light subtracted is given in Appendix A.

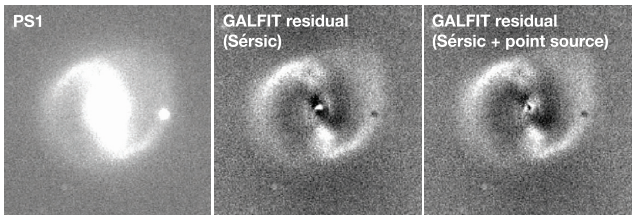

Figure 7. Left: PanSTARRS *g*-band image of the host galaxy. North is up, and east is towards the left of the image. We fit a Sérsic function for the overall surface brightness profile using GALFIT, but make no attempt to model the spiral arms. The model also includes a point source for the nearby star to the west, and optionally a central point source for the galactic nucleus. Middle: subtraction residuals without a central point source. Right: subtraction residuals when including a central point source. We find visibly smoother residuals in this case.

Using relations between velocity dispersion and black hole mass (the $M_\bullet - \sigma$ relation), this gives an SMBH mass $\log(M_\bullet/M_\odot) = 5.75 \pm 0.45$ in the calibration of McConnell & Ma (2013), or $\log(M_\bullet/M_\odot) = 6.52 \pm 0.34$ in the calibration of Kormendy & Ho (2013). The calibration of Gültekin et al. (2009) gives an intermediate value $\log(M_\bullet/M_\odot) = 6.18 \pm 0.44$. The reason for the large spread in these estimates is that these relations were calibrated based on samples that comprised mostly black holes more massive than 10^7 $M_\odot$. However, the estimates here are consistent, within the errors, with an independent mass measurement based on the TDE light curve (Section 5).

4.3 Host SED model

Archival photometry of this galaxy is available from the PanSTARRS catalogue in the *g*, *r*, *i*, *z*, *y* filters, as well as in data releases from the 2 Micron All Sky Survey (2MASS; Skrutskie et al. 2006) in the *J*, *H*, *K* filters, and the *Wide-field Infrared Survey Explorer* (*WISE*; Wright et al. 2010) in the *WISE* bands *W*1–*W*4. We retrieved the Kron magnitudes from PanSTARRS, the extended profile-fit magnitudes ('m_ext') from 2MASS, and the magnitudes in a 44 arcsec circular aperture (chosen to fully capture the galaxy flux) from WISE.

We fit the resultant spectral energy distribution (SED) with stellar population synthesis models in PROSPECTOR (Leja et al. 2017) to derive key physical parameters of the galaxy. The free parameters in our model are stellar mass, metallicity, the current star-formation rate and the widths of five equal-mass bins for the star-formation history, and three parameters controlling the dust fraction and reprocessing (see Leja et al. 2017 for details). Leja et al. (2017) identify important degeneracies between age–metallicity–dust, and the dust mass–dust attenuation curve. PROSPECTOR is specifically designed to account for such degeneracies in parameter estimation using Markov chain Monte Carlo analysis to fully explore the posterior probability density. van Velzen et al. (2020) also used PROSPECTOR to model this galaxy (but only the PanSTARRS data); the mass and metallicity we find using the full SED are consistent with their results, within the uncertainties. A difference in our modelling is that we allow for a non-parametric star-formation history to better understand the age of the system.

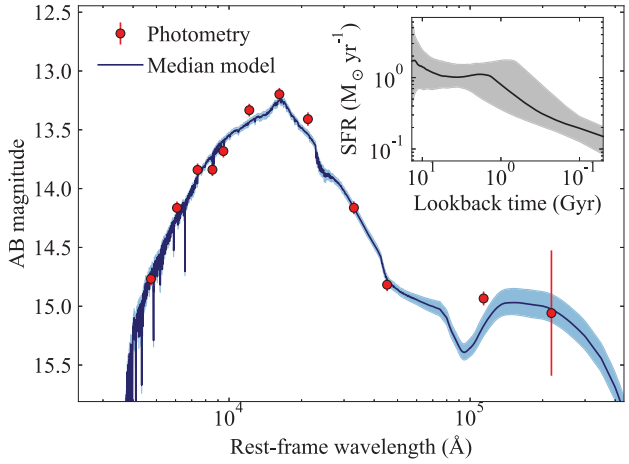

Figure 8. Archival photometry of the host galaxy, and SED fit using PROSPECTOR. The best-fitting model, as well as the 1σ dispersion in model realizations, is shown. The inset shows the derived star-formation history, which is approximately flat at 1–2 $M_\odot$ yr^{-1} prior to a steep drop in the last $\sim$1 Gyr.

The best-fitting model is shown compared to the archival photometry in Fig. 8. We find stellar mass $\log(M_*/M_\odot) = 10.26^{+0.12}_{-0.15}$, a subsolar metallicity $\log Z/Z_\odot = -0.84^{+0.28}_{-0.34}$ (but see Section 4.4), and a low specific star formation rate $\log \mathrm{sSFR} = -11.21^{+0.23}_{-0.55}$ in the last 50 Myr, where the reported values and uncertainties are the median and 16th/84th percentiles of the marginalized posterior distributions. The model also prefers a modest internal dust extinction, $A_V = 0.16 \pm 0.04$ mag. The stellar mass reported by PROSPECTOR is the integral of the star-formation history, and so includes stars and stellar remnants. From our model we measure a 'living' mass fraction (i.e. stars still undergoing nuclear burning) of 0.58 ± 0.02.

In the same figure, we plot the median and 1σ uncertainty on the star-formation history derived from the fit versus lookback time since the big bang. We find a roughly constant star-formation rate of $\approx$2 $M_\odot$ yr^{-1}, prior to a sharp drop in the last $\approx$1.5 Gyr. A recent decline in star-formation is a common feature of TDE host galaxies, as evidenced by the over-representation of quiescent Balmer-strong galaxies (and the subset of post-starburst galaxies) among this population (Arcavi et al. 2014; French, Arcavi & Zabludoff 2016; French et al. 2020a). Spectroscopy of the host after the TDE has completely faded will be required to confirm whether this galaxy is also a member of this class.

4.4 Galaxy emission lines and evidence for an AGN

The metallicity preferred by PROSPECTOR would be very low for a galaxy of $\gtrsim 10^{10}$ $M_\odot$, though van Velzen et al. (2020) find similarly low metallicities for all TDE hosts in their sample, including AT2019qiz, from their SED fits. Spectroscopic line ratios provide a more reliable way to measure metallicity. The TDE spectra clearly show narrow lines from the host galaxy. We measure the fluxes of diagnostic narrow lines using Gaussian fits. Specifically, we measure H α, H β, [O III] λ5007, [O I] λ6300, [N II] λ6584, and [S II] $\lambda\lambda$6717, 6731. We report the mean of each of these ratios (averaged over the six X-shooter spectra) in Table 1. No significant time evolution is seen in the narrow-line fluxes. To estimate the metallicity, we use the N2 metallicity scale ([N II] λ6584/H α), adopting the calibration from Pettini & Pagel (2004), to find an oxygen abundance $12 + \log(\mathrm{O/H}) = 8.76 \pm 0.14$. This corresponds to a metallicity $Z/Z_\odot = 1.17$, more in keeping with a typical massive galaxy. However, this [N II] λ6584/H α ratio is outside the range used to calibrate the Pettini & Pagel (2004) relation, so this metallicity may not be reliable. Applying the calibration of Marino et al. (2013), valid over a wider range, we find a slightly lower metallicity of $12 + \log(\mathrm{O/H}) = 8.63$, consistent with solar metallicity.

Table 1. Host emission-line fluxes and BPT line ratios (Baldwin, Phillips & Terlevich 1981), averaged over the X-shooter spectra.

Line	Flux (10^{-16} erg s^{-1} cm^{-2})
H β	7.9 $\pm$ 1.7
[O III] λ5007	8.0 $\pm$ 3.1
[O I] λ6300	$<$3.0
H α	14.2 $\pm$ 3.8
[N II] λ6584	7.6 $\pm$ 1.9
[S II] $\lambda\lambda$6717, 6731	6.3 $\pm$ 1.0
	log ratio
[O III] / H β	0.04 $\pm$ 0.25
[N II] / H α	$-$0.25 $\pm$ 0.14
[S II] / H α	$-$0.32 $\pm$ 0.16
[O I] / H α	$\lesssim -0.7$

Ratios of these lines are used in the Baldwin–Phillips–Terlovich (BPT) diagram (Baldwin et al. 1981) to probe the ionization mechanism of the gas. The ratios we measure for the host of AT2019qiz (Table 1) lie intermediate between the main sequence of star-forming galaxies and galaxies with ionization dominated by an active galactic nucleus (AGN). This could be evidence of a weak AGN, or another source of ionization such as supernova shocks or evolved stars (Kewley et al. 2001). Several other TDE hosts lie in a similar region of the BPT parameter space (Wevers et al. 2019a; French et al. 2020a), while a number show direct evidence of AGN ionization (Prieto et al. 2016). We note the caveat that if the lines in our spectra are excited by AGN activity, the calibrations used to estimate the metallicity may not always be valid.

To test the AGN scenario, we look at the mid-infrared colours. Stern et al. (2012) identify a colour cut $W1 - W2 > 0.8$ Vega mag to select AGN from WISE data. For the host of AT2019qiz, we find $W1 - W2 \approx 0$ Vega mag. At most a few per cent of AGN have such a blue $W1 - W2$ colour (Assef et al. 2013). Wright et al. (2010) employ a two-dimensional cut using the $W1 - W2$ and $W2 - W3$. The host of AT2019qiz has $W2 - W3 = 1.8$ mag, consistent with other spiral galaxies. Thus the emission detected by WISE is dominated by the galaxy, not an AGN.

The ratio of X-ray to [O III] luminosity can also be used as an AGN diagnostic. Converting the X-rays to the 2-20 keV band using our best-fit power-law, we measure a mean $L_X/L_{[\mathrm{O\,III}]} = 2.4 \pm 0.2$, which is consistent with a typical AGN (Heckman et al. 2005). However, the X-ray luminosity is only 0.03 per cent of the Eddington luminosity for an SMBH of 10^6 $M_\odot$. Moreover, the temporal variation in the luminosity and hardness of the X-rays during the flare suggests a significant fraction of this emission comes from the TDE itself, rather than an existing AGN. In particular, the softening of the X-rays could indicate that as time increases, more of the emission is coming from the TDE flare, relative to an underlying AGN with a harder spectrum. Taking into account the BPT diagram, WISE colours, X-rays, and the morphology of the nucleus (Section 4.1), we conclude that there is some support for a weak AGN, but that the galaxy is dominated by stellar light.

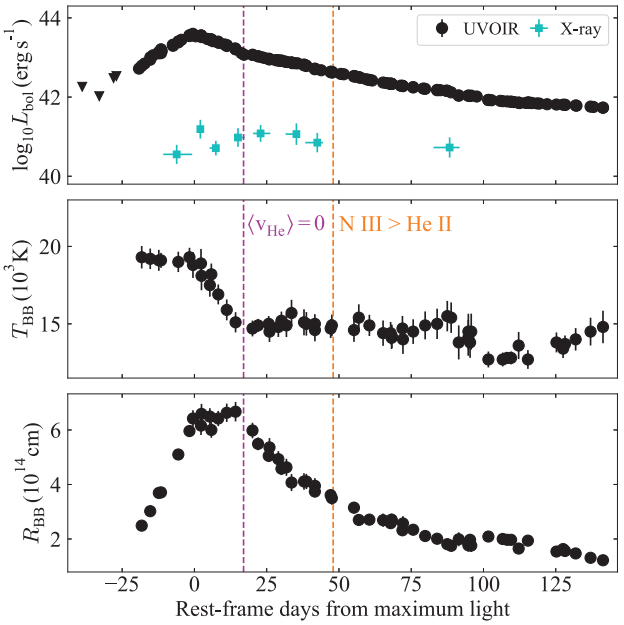

Figure 9. Top: bolometric light curve of AT2019qiz derived from UV and optical photometry. The X-ray light curve is also plotted, which is $\approx 10^3$ times fainter than the optical luminosity at peak but slower to fade. Middle: temperature evolution. Bottom: evolution of the blackbody radius. The temperature and radius are only shown for epochs covered without extrapolation by data in at least three photometric bands. Vertical lines indicate epochs of transition in the TDE spectrum, when the net blueshift of He II goes to zero and when N III becomes prominent (Section 6).

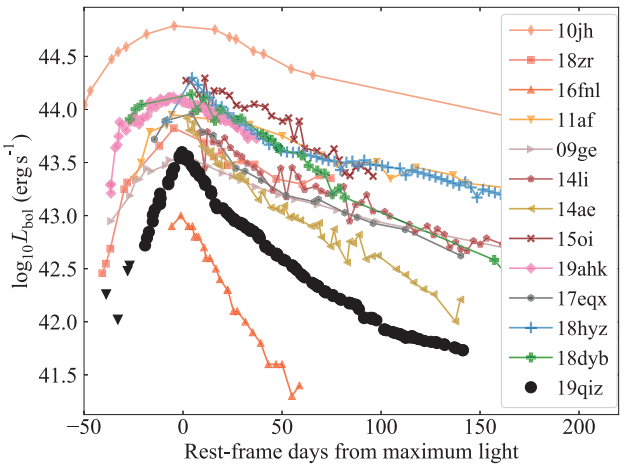

Figure 10. Comparison of the bolometric light curve to other TDEs from the literature (Gezari et al. 2012; Arcavi et al. 2014; Chornock et al. 2014; Holoien et al. 2014, 2016a,b; Blagorodnova et al. 2017; Leloudas et al. 2019; Nicholl et al. 2019b; van Velzen et al. 2019; Gomez et al. 2020)

5 PHOTOMETRIC ANALYSIS

5.1 Bolometric light curve

We construct the bolometric light curve of AT2019qiz by interpolating our photometry in each band to any epoch with data in the *g*, *r* or *o* bands, using SUPERBOL (Nicholl 2018). We then integrate under the spectral energy distribution inferred from the multicolour data at each epoch, and fit a blackbody function to estimate the temperature, radius, and missing energy outside of the observed wavelength range. A blackbody is an excellent approximation of the UV and optical emission from TDEs (e.g. van Velzen et al. 2020). However, we note that the radius is computed under the assumption of spherical symmetry, which may not reflect the potentially complex geometry in TDEs. We include foreground extinction, but do not correct for the uncertain extinction within the host galaxy (formally, this makes our inferred luminosity and temperature curves lower limits). The bolometric light curve, temperature and radius evolution are plotted in Fig. 9.

From the light curve we derive a peak date of MJD 58764 ± 1 (2019-10-08 UT),[7] a peak luminosity of $L = 3.6 \times 10^{43}$ erg s^{-1}, and integrated emitted energy of $E_{\rm rad} = 1.0 \times 10^{50}$ erg. Taking the black hole mass derived in Section 4, the peak luminosity corresponds to $\sim 0.2 L_{\rm Edd}$, where $L_{\rm Edd}$ is the Eddington luminosity. We also plot the X-ray light curve to highlight the X-ray to optical ratio, which is $10^{-2.8}$ before peak. Since the X-rays appear to rise after the optical emission starts to fade, this ratio increases to $\approx 10^{-2.0} - 10^{-1.8}$ between 20–50 d after bolometric peak, and reaches $\approx 10^{-1.4}$ beyond 50 d.

[7]The UV peaks slightly earlier (MJD 58764) than the optical (MJD 56766).

We plot the bolometric light curve compared to other well-observed TDEs in Fig. 10. The fast rise (and decline), and low peak luminosity place it intermediate between the bulk of the TDE population and the original 'faint and fast' TDE, iPTF16fnl (Blagorodnova et al. 2017; Brown et al. 2018; Onori et al. 2019).

The pre-maximum-light photospheric radius and temperature are unusually well constrained in AT2019qiz due to the early detections and multicolour photometry. The temperature is initially constant at ≈20 000 K before the light curve peaks, and then suddenly declines to ≈15 000 K over a period of ∼20 d. It stays constant for the remainder of our observations, barring a possible slight dip around day 100 (though at this phase the UV data are noisier due to the large fractional host contribution that has been subtracted).

The blackbody radius grows linearly up to maximum light, with a best-fit velocity of 2200 km s^{-1} (Fig. 11). Extrapolating back to radius $R = 0$ implies a time of disruption 30.6 d before peak. The radius then remains constant during the cooling phase identified in the temperature curve, before decreasing smoothly at constant temperature.

We fit the rising light curve with a power-law of the form $L = L_0((t - t_0)/\tau)^\alpha$ using the CURVE_FIT function in SCIPY. We fix the initial time $t_0 = 30.6$ d, as inferred from the expanding photosphere (we find a near-identical fit to the light curve even if t_0 is left free). The best fit has a rise time-scale $\tau = 10.9$ d and $\alpha = 1.99 \pm 0.01$. We plot this fit alongside the fit to the radius in Fig. 11. Holoien et al. (2019b) modelled the rise of the TDE AT2019ahk, detected very soon after disruption, and also found a power-law consistent with $\alpha \approx 2$. Hinkle et al. (2020) recently observed similar behaviour in the TDE AT2019azh.

We fit the declining light curve with a power-law function of the same form. As shown in the lower panel of Fig. 11, we find a best-fitting $\alpha = -2.54$, which is steeper than the canonical $L \propto t^{-5/3}$ predicted by simple fallback arguments (Rees 1988). However, this is not unusual among the diverse array of TDEs in the growing observed sample, and more recent theoretical work does not find a universal power-law slope for the mass return rate, nor that the light curve exactly tracks this fallback rate (e.g. Guillochon & Ramirez-Ruiz 2013; Gafton & Rosswog 2019).

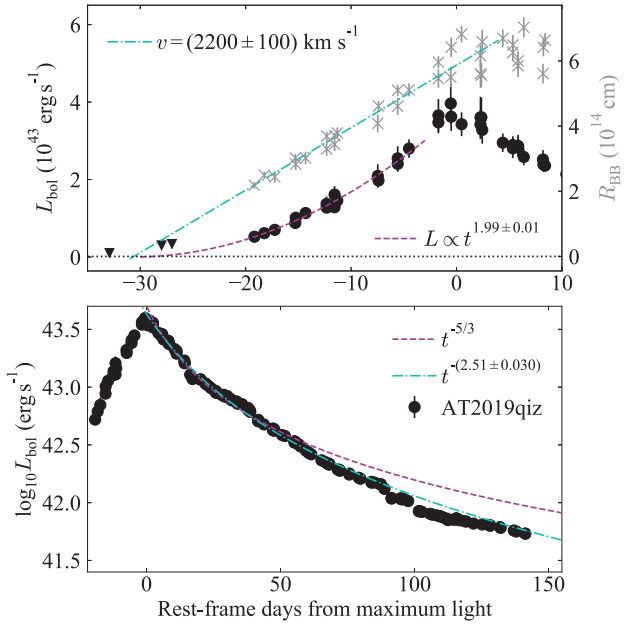

Figure 11. Power-law fits to the light curve. Top: the photospheric radius (grey crosses) before maximum light grows linearly with a velocity $v \approx 2200\,{\rm km\,s^{-1}}$, while the luminosity (black circles) is best fit as $L \propto t^2$. Bottom: the declining light curve is steeper than the canonical $t^{-5/3}$.

5.2 TDE model fit

To derive physical parameters of the disruption, we fit our multiband light curves using the Modular Open Source Fitter for Transients (MOSFIT; Guillochon et al. 2018) with the TDE model from Mockler, Guillochon & Ramirez-Ruiz (2019). This model assumes a mass fallback rate derived from simulated disruptions of polytropic stars by an SMBH of $10^6\,{\rm M}_\odot$ (Guillochon et al. 2014), and uses scaling relations and interpolations for a range of black hole masses, star masses, and impact parameters. The free parameters of the model, as defined by Mockler et al. (2019), are the masses of the black hole, $M_\bullet$, and star, M_*; the scaled impact parameter b; the efficiency ϵ of converting accreted mass to energy; the normalization and power-law index, $R_{\rm ph,\,0}$ and $l_{\rm ph}$, connecting the radius to the instantaneous luminosity; the viscous delay time T_v (the time taken for matter to circularize and/or move through the accretion disc) which acts approximately as a low pass filter on the light curve; the time of first fallback, t_0; the extinction, proportional to the hydrogen column density $n_{\rm H}$ in the host galaxy; and a white noise parameter, σ. The priors follow those used by Mockler et al. (2019), and reflect the range of SMBH masses where optically bright TDEs are expected (e.g. van Velzen 2018), the range of impact parameters covering both full and partial disruptions, accretion efficiencies for non-rotating to maximally rotating black holes, and a broad range of possible photospheres and viscous time-scales (see Mockler et al. 2019 for details).

The fits are applied using a Markov Chain Monte Carlo (MCMC) method implemented in EMCEE (Foreman-Mackey et al. 2013) using the formalism of Goodman & Weare (2010). We burn in the chain for 10 000 steps, and then continue to run our simulation until the potential scale reduction factor (PSRF) is <1.1, indicating that the fit has converged. We plot 100 realizations of the Markov Chain in the space of our light-curve data in Fig. 12. The model provides a good fit to the optical bands, but struggles slightly to resolve the sharp peak present in the UV bands.

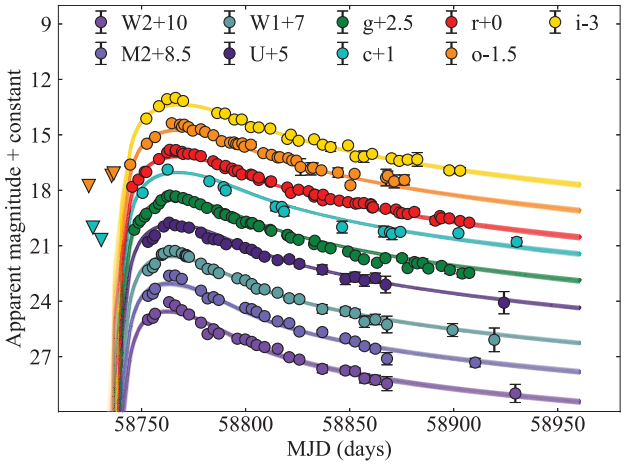

Figure 12. Fits to the multicolour light curve using the TDE model in MOSFIT (Guillochon et al. 2018; Mockler et al. 2019).

Table 2. Priors and marginalized posteriors for the MOSFIT TDE model. Priors are flat within the stated ranges, except for M_*, which uses a Kroupa initial mass function. The quoted results are the median of each distribution, and error bars are the 16th and 84th percentiles. These errors are purely statistical; Mockler et al. (2019) provide estimates of the systematic uncertainty.

Parameter	Prior	Posterior	Units
$\log(M_\bullet)$	[5, 8]	$5.89^{+0.05}_{-0.06}$	$M_\odot$
M_*	[0.01, 100]	0.97 ± 0.04	$M_\odot$
b	[0, 2]	$0.22^{+0.02}_{-0.03}$	
$\log(\epsilon)$	[−2.3, −0.4]	$-2.23^{+0.14}_{-0.05}$	
$\log(R_{\rm ph,\,0})$	[−4, 4]	1.12 ± 0.06	
$l_{\rm ph}$	[0, 4]	0.66 ± 0.03	
$\log(T_v)$	[−3, 3]	$0.74^{+0.05}_{-0.06}$	d
t_0	[−50, 0]	$-7.04^{+0.52}_{-0.60}$	d
$\log(n_{\rm H,\,host})$	[19, 23]	$20.03^{+0.26}_{-0.48}$	cm^{-2}
$\log\sigma$	[−4, 2]	-0.72 ± 0.02	

From this fit we derive the posterior probability distributions of the parameters, listed in Table 2, with two-dimensional posteriors plotted in Appendix B. The inferred t_0 is MJD 58737 ± 1, i.e. 27 ± 2 d before peak, consistent with the simpler power-law models. This suggests that the first detection of AT2019qiz is about a week after the beginning of the flare. The physical parameters point to the disruption of a roughly solar mass main-sequence star by a black hole of mass $10^{5.9}\,{\rm M}_\odot$. This is consistent with the lower end of the SMBH mass range estimated from spectroscopy and the $M_\bullet$–σ relation. In this case, the peak luminosity corresponds to $0.36 L_{\rm Edd}$ (the Eddington luminosity). This is consistent with the typical Eddington ratios measured for a sample of TDEs with well-constrained SMBH masses (Wevers et al. 2019a).

The scaled impact parameter, $b = 0.22 \pm 0.02$, corresponds to a physical impact parameter $\beta \equiv R_{\rm t}/R_{\rm p} = 0.86 \pm 0.03$, where $R_{\rm t}$ is the tidal radius and $R_{\rm p}$ the orbital pericentre. For the inferred SMBH mass, $R_{\rm t} = 23 R_{\rm S}$, where $R_{\rm S}$ is the Schwarzschild radius. Using the remnant mass versus β curve from Ryu et al. (2020) for a $1\,{\rm M}_\odot$ star, up to ~ 25 per cent of the star could have survived this encounter. Interestingly, Ryu et al. (2020) predict a mass fallback rate proportional to $t^{-8/3}$ in this case (which they call a 'severe partial disruption'), which is remarkably close to our best-fitting power-law decline, $t^{-2.54}$.

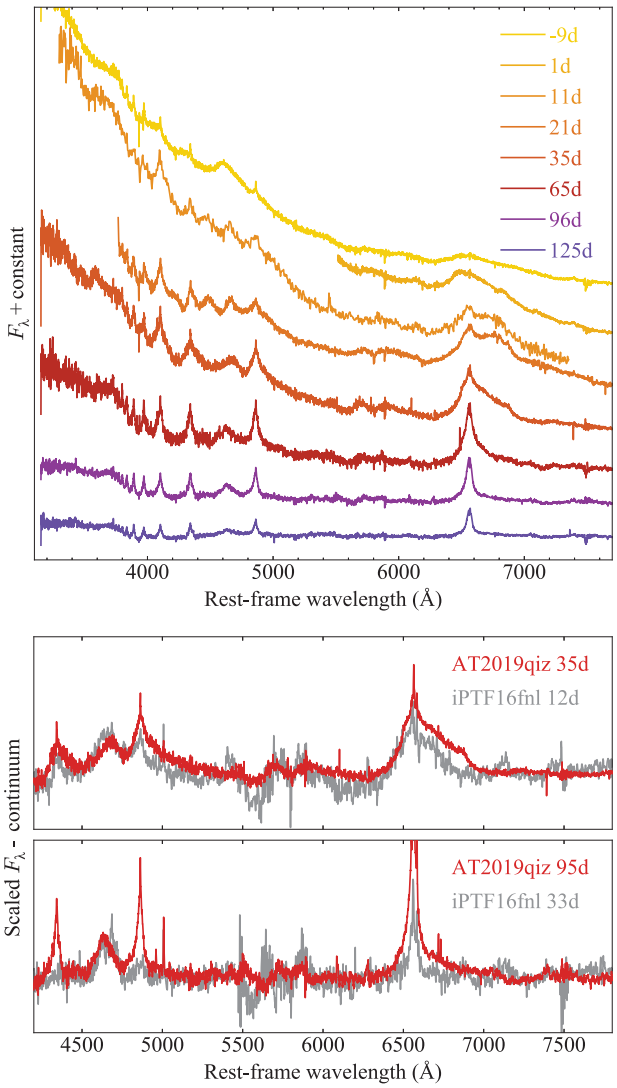

Figure 13. Top: selected spectra from X-shooter, EFOSC2, and Binospec after subtraction of the host galaxy model (following the method outlined in the appendix). We have applied the subtraction procedure to all spectra, but here show only this subset (spanning the full range of observed phases) for clarity. Bottom: Comparison of AT2019qiz to X-shooter spectra of iPTF16fnl (from Onori et al. 2019), the only TDE with a faster light-curve evolution than AT2019qiz. The continuum has been removed using polynomial fits. The spectra shortly after maximum light are quite similar for these two events, though the Balmer lines are much weaker at late times in iPTF16fnl.

6 SPECTROSCOPIC ANALYSIS

The early spectra are dominated by a steep blue continuum indicative of the high photospheric temperature (15 000–20 000 K), superposed with broad emission bumps. As the spectra evolve and the continuum fades, the emission lines become more sharply peaked, while the host contribution becomes more prominent. In all the analysis that follows, we first subtract the host galaxy light using the model SED from PROSPECTOR (Section 4). The full set of host-subtracted spectra, along with further details of the subtraction process, is shown in Appendix A. In Fig. 13, we plot a subset of high signal-to-noise ratio, host-subtracted spectra spanning the evolution from before peak to more than 100 d after.

6.1 Line identification

To focus on the line evolution, we subtract the continuum using a sixth-order polynomial, with sigma-clipping to reject the line-dominated regions during the fit. The host- and continuum-subtracted spectra obtained with X-shooter are shown in Fig. 14 (only this subset is shown for clarity of presentation). We identify and label the strong emission lines from both the TDE and the host galaxy. PROSPECTOR allows to the user to turn nebular emission lines on and off; for the bulk of our analysis we use the predictions from PROSPECTOR to subtract nebular lines, but in Fig. 14 we leave the nebular emission in our data for completeness. Balmer emission lines are at all times visible, with both a broad TDE component and a narrow host component. The other strong host lines are those used for the BPT analysis in Section 4.

As well as hydrogen, we also identify broad emission lines of He II λ4686, the Bowen fluorescence lines of N III λ4100 and λ4640 and likely O III λ3670 (Bowen 1935; Blagorodnova et al. 2019; Leloudas et al. 2019), and possible weak emission of He I λ5876. The combination of hydrogen lines with the He II/Bowen blend at around 4600 Å is common in TDE spectra, and qualify AT2019qiz as a TDE-Bowen in the recent classification scheme proposed by van Velzen et al. (2020), or an N-rich TDE in the terminology of Leloudas et al. (2019).

In our light-curve comparison, we found that AT2019qiz appeared fainter and faster than nearly any other TDE except for iPTF16fnl (see also Section 7.2 for a more quantitative discussion). We plot a spectroscopic comparison in the lower panel of Fig. 13. The spectrum of AT2019qiz at about a month after maximum shows several similarities to iPTf16fnl at a slightly earlier phase of 12 d, particularly in the blue wing of Hα, though AT2019qiz exhibits a broader red wing. The ratio of Hα compared to He II is also quite consistent between these two events, modulo the slower evolution in AT2019qiz. At later times, the Balmer lines become weaker in iPTF16fnl, though Hα narrows and becomes more symmetric, as we see in AT2019qiz. In fact, the ratios and velocity profiles of these lines evolve substantially with time, as we saw in Fig. 14. We will now investigate this in detail in the following sections.

6.2 The Hα profile

We look first at the Hα line. This region of the spectrum is plotted in velocity coordinates in Fig. 15. We have subtracted the continuum locally using a linear fit to line-free regions at either side of the line (6170–6270 Å, 7100–7150Å). The Hα profile is initially asymmetric and shallow, with a blueshifted peak and a broad red shoulder. The red side may include some contribution from He I λ6678, but this is likely not a major contributor as we see only very weak He I λ5876. We initially fit the profile as the sum of two Gaussians whose normalizations and velocity widths vary independently, with one centroid fixed at zero velocity and the other free to vary. The three velocities (two widths and one offset) are plotted in Fig. 15.

We find that the zero-velocity component is at all times narrower than the offset component, and over time decreases in width as the line becomes sharply peaked. The asymptotic velocity full width at half-maximum (FWHM) is $\approx$2000 km s^{-1}. The broader component is always redshifted, though this shift decreases as the red shoulder becomes less prominent. This component maintains a width of $\sim$15 000 km s^{-1}, though the scatter in measuring this component is quite large at later times when the shoulder is less prominent. We confirm that this feature is not a blend with He I, as the velocity offset does not match the wavelength of that line (and varies over time).

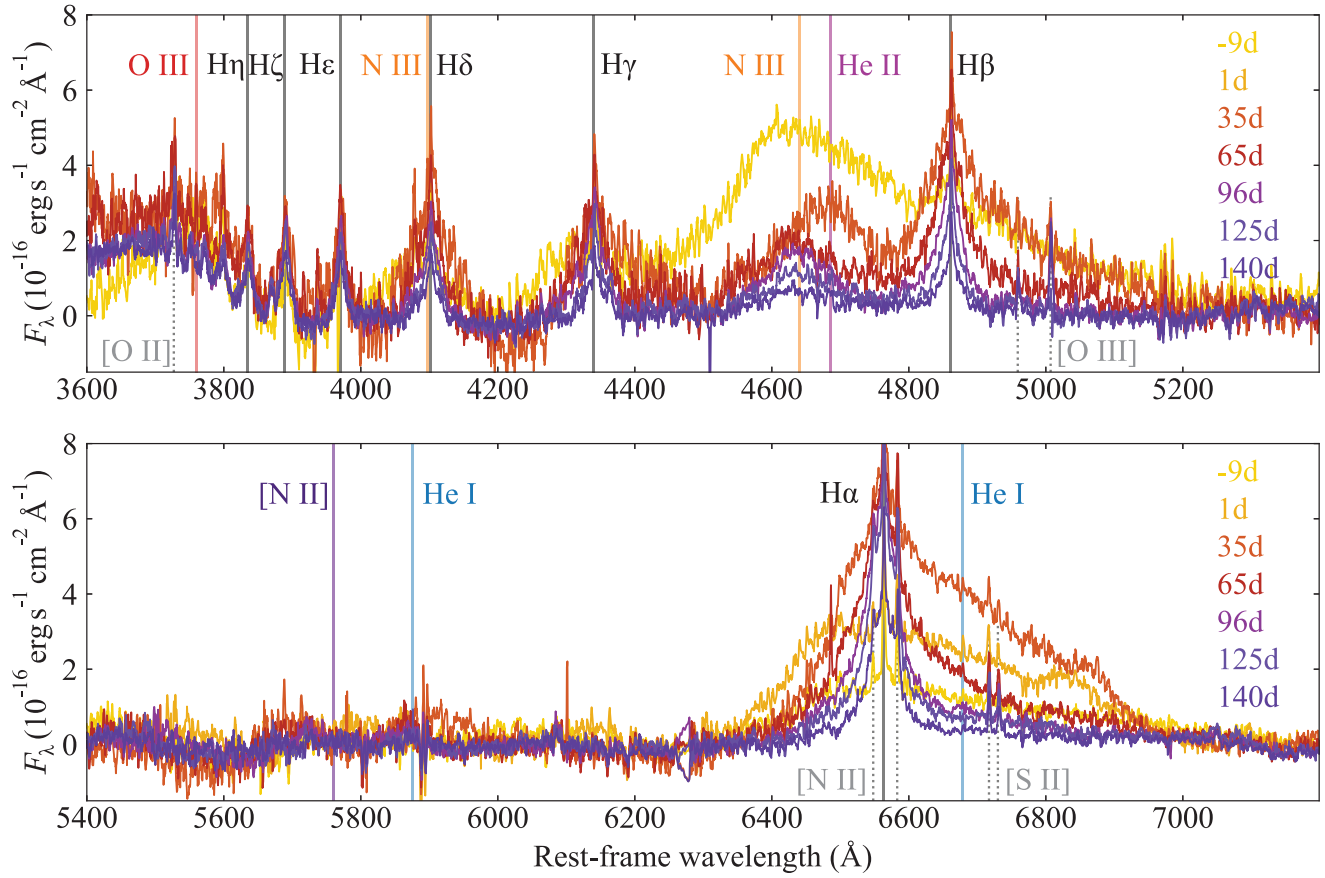

Figure 14. Host-subtracted X-shooter spectra after fitting and subtracting the continuum to highlight the emission lines. All strong lines from the TDE (solid coloured lines) and nebular emission in the host galaxy (grey dotted lines) are labelled. Note that the higher-order Balmer lines (Hϵ, etc.) and continuum bluewards of ∼4000 Å may not be reliable, as we lack pre-disruption photometry to constrain the host galaxy model at these wavelengths.

If the broadening of the redshifted component is due to rotation, the implied radius of the emitting material is $\approx 200 R_S \approx 5 - 10 R_p$. This is consistent with the size of TDE accretion discs in the simulations of Bonnerot & Lu (2020). Disc profiles in TDE emission lines have been claimed in PT09djl (Arcavi et al. 2014; Liu et al. 2017) and AT2018hyz (Hung et al. 2020; Short et al. 2020). However the difficulty in interpreting these line profiles is illustrated by the case of AT2018zr (also called PS18kh), which had flat-topped Balmer lines argued by Holoien et al. (2019a) to originate in an elliptical disc and by Hung et al. (2019) to instead come from an outflow. AT2019qiz does not show a classic flat-topped or 'double-horned' disc profile at early or late phases, though it is interesting to note that around 20 d after maximum (e.g. Fig. 13), the red shoulder temporarily resembles a second peak, with the blue peak close to rest wavelength.

To produce this profile with a disc model would require a highly elliptical disc, viewed close to edge on and with a near-vertical orientation of the pericentre with respect to the observer, as was suggested to be the case for PT09djl by Liu et al. (2017). If we were to interpret the day 20 Hα profile of AT2019qiz as a disc, it would be surprising to find the same highly specific geometry in two out of four TDEs with claimed disc signatures. On the other hand the transient appearance of a double-peaked profile at this phase after peak would be reminiscent of AT2018hyz. The transience of these signatures could be due to either optical depth effects (Gomez et al. 2020; Short et al. 2020) or contamination by an additional emission component (Hung et al. 2020). Detailed time-series modelling with disc profiles will be needed to confirm if this scenario is compatible with AT2019qiz.

Alternatively, this redshifted component could correspond to emission from the receding part of an outflow, and a Gaussian or double-Gaussian profile may be an oversimplification. Roth & Kasen (2018) (hereafter, RK18) calculated line profiles including the effects of electron scattering above a hot photosphere in an outflowing gas. Qualitatively, their models show properties similar to AT2019qiz: a blueshifted peak (seen here only at early times) and a broad red shoulder. A decreasing optical depth or velocity in these models leads to a narrow core. We compare the observed Hα profiles in Fig. 15 to models from RK18, but we find that the implied velocity from the data is lower than any of the available models, apart from in the earliest epochs where a model with $v = 5000\,\mathrm{km\,s^{-1}}$ gives an acceptable match. We will return to the early-time line profile in detail in Section 6.5.

We fit the Hα profiles again, this time as a sum of a Gaussian centred at zero velocity (as before) and the $v = 5000\,\mathrm{km\,s^{-1}}$ outflow model from RK18. The zero-velocity component could correspond to emission from pre-existing gas, since the RK18 profile should account for the TDE emission self-consistently. The only free parameter for the outflow component is the normalization of the RK18 spectrum. This gives a good fit at early ($\lesssim$ 0 d) and late ($\gtrsim$ 50 d) times, but gives an inferior fit around 30 d compared to the double-Gaussian model. We note that the published model assumed a photospheric radius of 2.7×10^{14} cm, similar to the blackbody

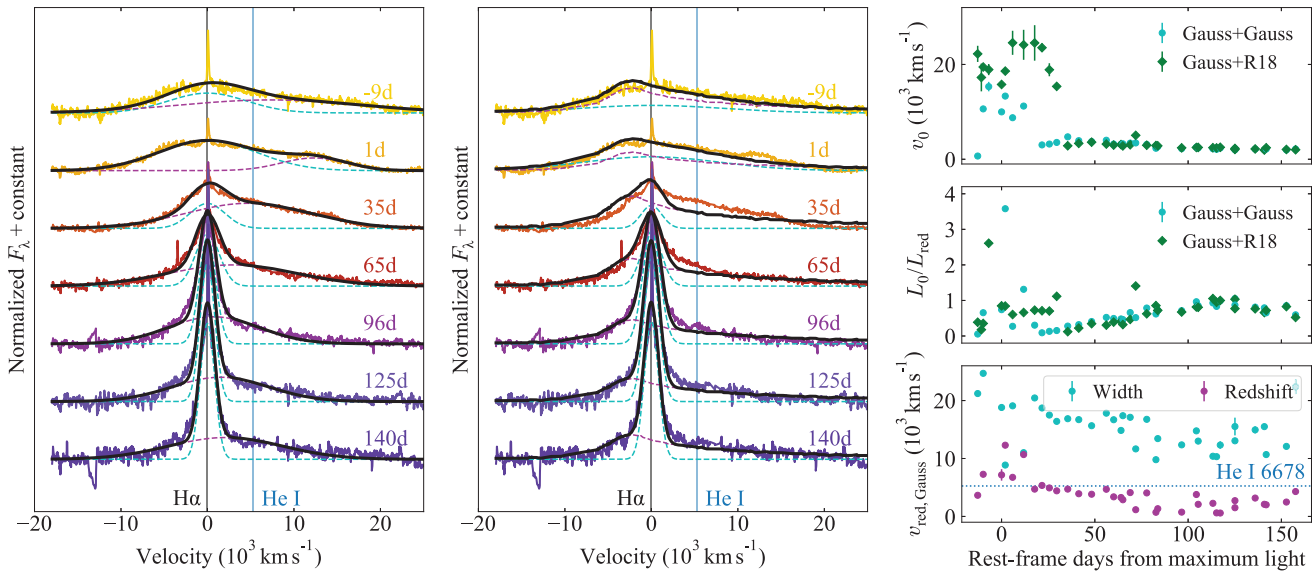

Figure 15. Left: double-Gaussian fits to the continuum-subtracted H α line profile (only X-shooter spectra shown for clarity). One component is fixed around zero velocity with a variable width, while the other can vary in both width and red-/blueshift. The summed profile is shown as a solid line, while the fixed-centre and shifted profiles are shown as dotted lines. Middle: same as left, but the offset component is now replaced with a 5000 km s^{-1} outflow profile from Roth & Kasen (2018). Right: Velocity and flux measurements from fits. The component with a fixed centre at zero velocity exhibits a similar evolution in both the double-Gaussian (left) and Gaussian+outflow (middle) models. In the former, this component is at all times narrower than the redshifted component (bottom panels). The broad component is not consistent with He I λ6678 (at various times it is centred at either too high or too low velocity). The flux ratio of the narrow component to the offset/outflow component increases over time from ∼0.5 to ∼1 for both models.

radius of AT2019qiz well before and after peak, whereas at peak the radius of AT2019qiz is a factor of $\gtrsim 2$ larger, which may explain this discrepancy. As is shown in Fig. 15, the velocity of the Gaussian core, and the ratio of luminosity between the broad component and the zero-velocity component, are comparable between the double-Gaussian and Gaussian+RK18 fits.

In both models, when the narrow core of the line is revealed at late time we measure $v \approx 2000$ km s^{-1}. Rather than line emission from the TDE itself, an alternative interpretation of the line profile is a pre-existing broad-line region (BLR) illuminated by the TDE (recalling that this galaxy shows evidence for hosting an AGN; Section 4). Interpreting the width of the narrow component as a Keplerian velocity would yield an orbital radius $\approx 5 \times 10^{15}$ cm ($\approx 10^4$ Schwarzschild radii, R_S). We note that an outflow from the TDE can reach this distance and interact with a BLR within 100 d if the expansion velocity is $\gtrsim 6000$ km s^{-1}.

At least one previous TDE in a galaxy hosting an AGN has shown evidence of lighting up an existing BLR (PS16dtm; Blanchard et al. 2017), and further candidates have been discovered (Kankare et al. 2017). Although the narrow core of the Balmer lines is therefore quite plausibly associated with a BLR, it is difficult to interpret the entire line evolution in this way. The red wing does not decrease significantly in velocity over time, as it should if the emission is coming from material progressively further out (i.e. with a lower orbital velocity). Moreover, AGN BLRs do not produce the very strong, broad, asymmetrical He II and Bowen lines that co-exist with the broad early component of He I, and which we now discuss.

6.3 The 4650 Å He-Bowen blend

Next we examine the He II region of the spectrum. This is complicated by a blend of not only He II λ4686 and N III λ4640, but also H β and H γ. In Fig. 16, we set zero velocity at the rest-frame wavelength of He II. The earliest spectra before maximum light show a single broad bump with a peak that is bluewards of both He II and N III. After maximum, the H β line becomes much more prominent, with a sharp profile similar to H α, while the broad bump fades and by ≈20 d after maximum is centred at zero velocity. This indicates the early emission is dominated by He II rather than N III. However as the spectra evolve this line moves back to the blue, and by ∼70 d is centred at the rest wavelength of N III. This is where it remains over the rest of our observations.

We quantify this by fitting this region with a sum of four Gaussians (He II, N III, H β, and H γ). All profiles are centred at zero velocity. The two Balmer lines are constrained to have the same width, and to make the problem tractable we also impose a further condition that the widths of He II and N III match each other. The fits are overlaid on Fig. 16, where we also show the evolution in luminosity of the He II and N III components. The luminosities of the two components are poorly constrained pre-peak, but by ∼20 d after peak the He II component is clearly dominant, with almost no contribution from N III. Soon afterwards, the N III luminosity increases while that of He II drops, and by 50 d N III is the dominant component, with no significant He II flux detectable after $\gtrsim 60$ d.

Other TDEs have shown separate resolved components of He II and N III (Blagorodnova et al. 2019; Leloudas et al. 2019), however this transition from almost fully He II dominated to fully N III dominated is remarkable, particularly given that the Bowen mechanism is triggered by the recombination of ionized He II. Leloudas et al. (2019) measured the He II/N III ratio for four TDEs with confirmed Bowen features, of which the two with events with >2 epochs of measurement showed an increasing He II/N III up to at least 50 d, opposite to what we observe in AT2019qiz. One of these events, AT2018dyb, may have shown a turnover after 60 d, but this is based on only one epoch, and ASASSN-14li continued to increase its

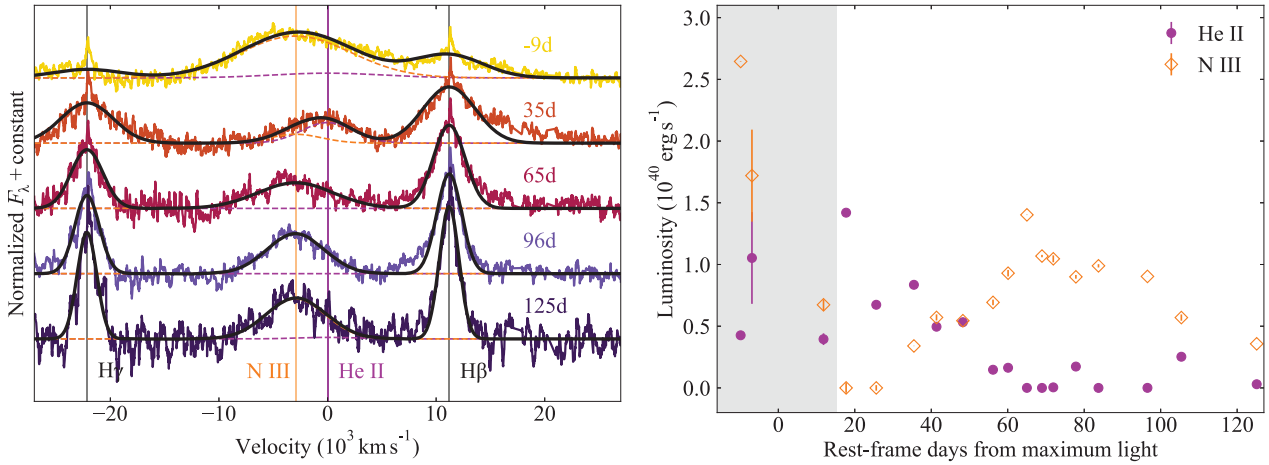

Figure 16. Left: Gaussian fits to the continuum-subtracted He II, N III, H β, and H γ line profiles (only X-shooter spectra shown for clarity). All lines are centred at their rest position. The velocity width of the two Balmer lines is constrained to be the same. We also impose that the widths of He II and N III must match each other to help the fit converge. The summed profile is shown as a solid line, while the He II and N III profiles are shown as dotted lines. Right: deblended luminosity evolution of He II and N III lines measured from Gaussian fits. The grey shaded region is where the peak of the blended feature is bluewards of N III, i.e. Gaussian fits do not well describe the blueshifted feature.

He II/N III ratio for at least 80 d after peak. Based on two epochs measured for iPTF16axa, it may have shown a decrease in He II/N III as in AT2019qiz.

One other TDE to date has shown a clear increase in N III while He II fades, as we see in AT2019qiz. Onori et al. (2019) analysed a series of X-shooter spectra of iPTF16fnl, and found that the ratio of He II/N III decreased from >5 to <1 over a period of ∼50 d, similar to the magnitude and time-scale of the evolution in AT2019qiz. Interestingly, we note that the measured He II/N III ratios are in tension with the simplest theoretical predictions for *all* TDEs in which Bowen lines have been detected. Netzer, Elitzur & Ferland (1985) calculated this ratio for a range of physical conditions appropriate for AGN, and found in all cases that $L_{\rm N\,III}/L_{\rm He\,II} \approx 0.4$–$0.85$. The reversal in this ratio in AT2019qiz, as well as iPTF16fnl (Onori et al. 2019), AT2018dyb (Leloudas et al. 2019), and iPTF15af (Blagorodnova et al. 2019), is a puzzle that requires the application of detailed line transfer calculations.

6.4 Balmer line ratios

Using the fits to this part of the spectrum and to H α, we calculate the ratios between the Balmer lines. For the H α luminosity we include both components in measuring the total flux (and we confirm that the luminosity derived from the fits matches that obtained by direct integration). For H β and H γ the fits include only one component, though at early times there may be a weak red shoulder visible in these lines too. The ratios are plotted in Fig. 17. There is no strong evidence for an evolution in the line ratio with time. We find H α/H $\beta \approx 4.7$ and H γ/H $\beta \approx 0.7$. These ratios are marginally consistent with photoionization and recombination (Osterbrock & Ferland 2006). This is what one would expect, for example, if the line emission is dominated by an AGN BLR. A moderate internal dust extinction of $E(B-V) \approx 0.5$ mag would bring the H α/H β ratio into agreement with the theoretical Case B value of 2.86, though we note that the light-curve analysis supports a lower extinction. The host galaxy modelling also favours a low (spatially averaged) extinction, as does the rather weak Na I D absorption. The equivalent widths of each line in the doublet ($D1 \approx D2 \approx 0.1$) correspond to $E(B-V) = 0.02$ in the calibration of Poznanski, Prochaska & Bloom (2012). However, the extinction could be significantly higher in the nucleus.

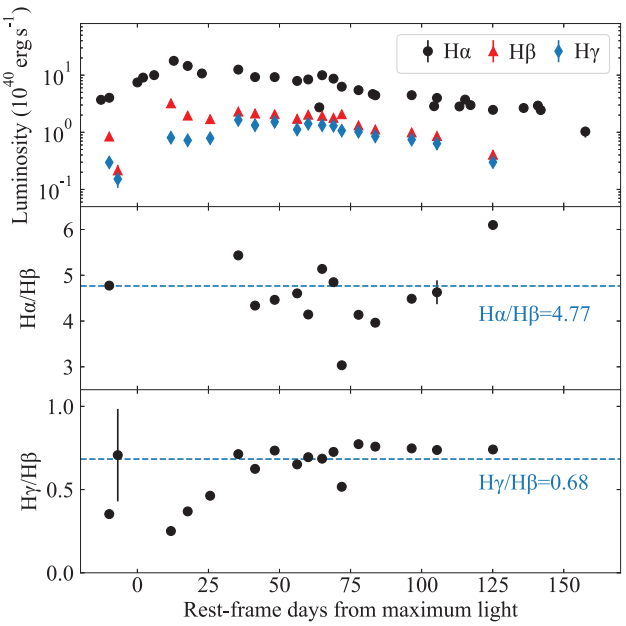

Figure 17. Luminosities and ratios of the Balmer emission lines as a function of time, measured using Gaussian fits. Dashed horizontal lines show the mean ratios. These have not been corrected for the (uncertain) extinction in the host galaxy.

It has recently been pointed out that a number of TDEs show much flatter Balmer decrements (H α/H $\beta \approx 1$; Leloudas et al. 2019; Short et al. 2020), which may indicate collisional excitation of these lines, e.g. in a disc chromosphere (Short et al. 2020). This ratio can be difficult to measure in TDEs due to line blending, but the excellent data quality available for AT2019qiz confirms a higher Balmer ratio in this event. If we assume a collisional origin for the Balmer lines in AT2019qiz, the implied temperature of the line-forming region is $\lesssim$3000 K, following Short et al. (2020). Alternatively, a large Balmer

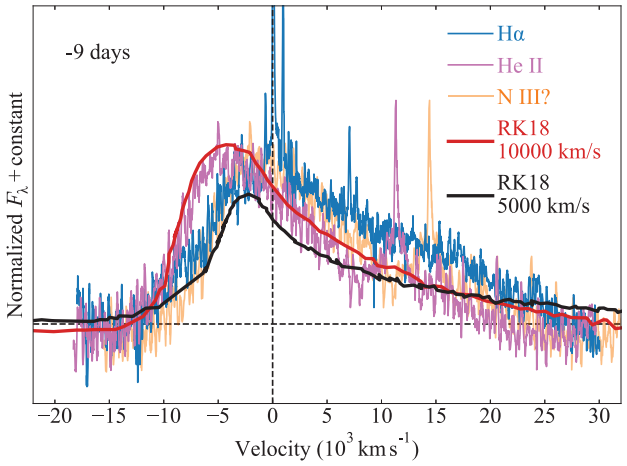

Figure 18. Velocity profiles of the strongest emission lines in the X-shooter spectrum at 9 d before peak, during the early rise/expansion phase. We show Hα, and the broad He II/Bowen bump for two different cases: (i) assuming that the line is dominated by He II (pink) or (ii) that it is dominated by N III (orange). Although the latter case gives a profile quite similar to Hα, the evolution over the next 20–30 d suggests that He II is more likely the dominant component. Overplotted are model line profiles from Roth & Kasen (2018). Assuming the blend is dominated by He II, an excellent match is found for a 10 000 km s^{-1} outflow. Hα comes from slower material with velocity $\lesssim$ 5000 km s^{-1}.

decrement may indicate shock powering, as is seen in many Type IIn supernovae (e.g. Smith et al. 2010).

Finally, we note that the spectra in Fig. 14 appear to show a positive Balmer jump (i.e. enhanced flux below the Balmer break at 3646 Å), though we caution again that this may be due to an unreliable host subtraction at short wavelengths. If the positive jump is real, this could signify an extended atmosphere, where the additional bound-free opacity below the Balmer break means that we observe a $\tau \sim 1$ surface at a larger radius, and hence see a larger effective emitting surface.

6.5 Outflow signatures in the pre-maximum spectrum

The analysis in Sections 6.2 and 6.3 suggested the early blueshifted line profiles may be indicative of an outflow. We make this more explicit here by comparing the Hα and He II/Bowen line profiles in our earliest X-shooter spectrum, obtained 9 d before maximum light. Fig. 18 shows these lines in velocity coordinates. We reiterate that at early times, the 4650 Å blend seems to be dominated by He II rather than N III (Fig. 16 and Section 6.3), but we plot the profile for both possible cases for completeness.

Both lines exhibit a peak blueshifted from their rest wavelengths (whether the 4650 Å feature is He II or N III). Assuming that the He II line is strongest at early times, we see that He II shows a larger blueshift than Hα. Both lines have a similar broad and smooth red shoulder. We quantify the velocity difference using the electron-scattering outflow models from RK18, previously applied only to Hα in Section 6.2. Line broadening in these models includes both the expansion and thermal broadening. We note the important caveat that these profiles were calculated explicitly only for Hα, but RK18 suggest that the qualitative results should apply to the other optical lines too. We proceed here under that assumption.

The fit to Hα with a 5000 km s^{-1} model (the lowest velocity published model) is indicative of an outflow but does not fully capture the shape of the red side of the line. Interpolating/extrapolating by eye between the parameters explored by RK18, we suggest that a larger optical depth and a slightly lower velocity would likely produce a closer match to the observed profile. Alternatively, a two-component model as explored in Fig. 15 can produce a satisfactory fit.

The He II line shows even stronger evidence for an outflow. This profile gives an excellent match to a 10 000 km s^{-1} outflow model from RK18 (with other parameters the same as the 5000 km s^{-1} model). If this line profile was instead N III dominated, the inferred velocity would be closer to that of Hα.

In our photometric analysis, we found that the blackbody photosphere of AT2019qiz initially expanded at a velocity $\gtrsim$ 2000 km s^{-1} (Fig. 11). This suggests a velocity gradient or homologously expanding outflow, where the line-forming region above has a greater velocity than the continuum photosphere below. This is consistent with the RK18 models, which assume a homologous velocity profile. We will discuss such a profile in detail in the next section.

In this context it is somewhat surprising that He II exhibits a larger velocity than Hα, as Roth et al. (2016) found that Hα should be emitted further out in radial coordinates than He II due to its greater self-absorption optical depth. In this case He II, emitted deeper in the debris, would experience a larger electron scattering optical depth. We speculate that degeneracies between electron scattering optical depth and velocity may be responsible for the apparent contradiction. Alternatively, this may indicate that N III is a better identification for this feature at both early and late times (though not at the phases where we clearly do see He II at zero velocity). This could be the case if the density in the line-emitting region is high enough for efficient operation of the Bowen mechanism at early and at late times, but not at intermediate phases ≈20–40 d after peak.

7 DISCUSSION

7.1 The outflow-dominated early evolution and the onset of accretion

As discussed in previous sections, the early optical (photospheric and emission line) evolution of AT2019qiz can be interpreted as a roughly homologous outflow. Fig. 19 illustrates such a profile, with the velocity gradient fixed at early times by the tight constraints on the expansion rate of the photosphere (Section 5), and the maximum velocity set by modelling of the optical emission lines ($v_{sc} \approx$ 10 000 km s^{-1}). Although this profile is likely a simplification of the messy geometry in a real TDE, it will serve as a useful reference in the discussion to follow.

The detection of blueshifted emission lines is not unique to AT2019qiz, with other TDEs exhibiting either blueshifted He II or asymmetric Hα profiles, as shown in a comparison with other TDE spectra in Fig. 20. However, due to its proximity allowing detection in the radio, we can unambiguously say that AT2019qiz launched an outflow. Preliminary modelling of the radio light curve (Alexander et al., in preparation) indicates that the velocity of radio-emitting material is $v_{radio} \approx 0.03c \approx$ 10 000 km s^{-1}. This consistency between optical- and radio-derived velocities strongly suggests that the optical line broadening is indeed a consequence of expansion, and therefore supports the picture that the complex line profiles in TDEs do – at least in some cases – form in outflowing gas (RK18).

The dense time-series spectroscopy of AT2019qiz and very early photometric data allow us to study how the outflow influences the optical rise of the TDE and determine the dominant power sources over the course of the light-curve evolution. We now combine our results from the optical, X-rays, and spectroscopy to examine each phase of the transient.

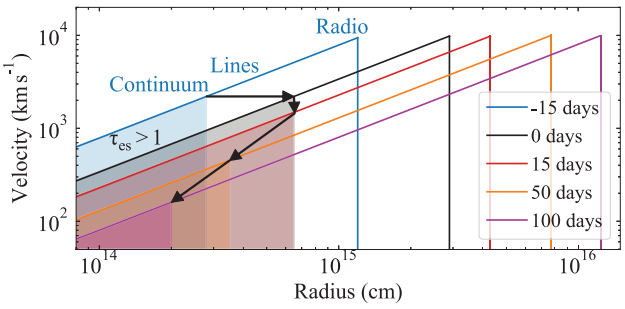

Figure 19. Representative snapshots in time of a homologous velocity profile that simultaneously describes our photometry, spectroscopy, and the radio detection. The slope is tightly constrained at phases $t \leq 0$ by the evolution of the photospheric radius (Fig. 11), which has $v_{ph} = 2200\,km\,s^{-1}$ and $R = 6.5 \times 10^{14}$ cm at maximum light. The scale (maximum) velocity of $v_{sc} \approx 10\,000\,km\,s^{-1}$ is derived from fitting the spectral lines. After maximum light, we assume that the ejecta continue to expand with this profile. We mark the *observed* radius of the photosphere (Fig. 9) at each epoch; the region below the photosphere (the reprocessing layer) is shaded. Line emission comes from the unshaded region, which has a characteristic size of $\sim 10^{15}$ cm, consistent with the parameters used by RK18 when modelling the line profiles. Radio emission comes from the leading edge of the ejecta shocking the ISM (Alexander, in preparation). The arrows highlight the movement of the photosphere: as it recedes to a smaller radius after maximum light, the bulk of the line-emitting region is at lower velocity. The X-ray emitting region resides at a much smaller radius ($\sim R_t \lesssim 10^{13}$ cm) not visible on this plot; X-rays must escape either through gaps in the reprocessing layer or a polar funnel (Dai et al. 2018).

7.1.1 *The constant-velocity phase*

The earliest detections of AT2019qiz are characterized by a power-law like rise to maximum light over a period of ≈35 d. During this time, the blackbody radius increases at a roughly constant velocity of $\gtrsim 2000\,km\,s^{-1}$, with no significant temperature evolution (Fig. 11). Blueshifted emission lines, with $v \sim 5000$–$10\,000\,km\,s^{-1}$ (Fig. 18), and a radio detection confirm the rapid expansion.

Generally, such an outflow would cool, but in a TDE we may have a complex trade-off between cooling through adiabatic expansion and heating through continuous energy injection. A quasi-spherical expansion or wind at a perfectly constant velocity and temperature would lead to a luminosity evolution $L \propto t^2$, consistent with the data. We also note that the mass return rate at early times may influence the shape of the rising light curve, and recent simulations find $\dot{M} \propto t^2$ during the second periapsis passage (Liptai et al., in preparation). A steeper power-law would indicate a non-spherical outflow: for example, the ballistic ejection of bipolar blobs which then undergo additional expansion due to their own internal pressure. This has been used to explain some observations of classical novae (Shore et al. 2018), but to our knowledge this geometry of mass ejection is not predicted by TDE simulations.

Several models predict a quasi-spherical outflow in TDEs, with $v \sim 10\,000\,km\,s^{-1}$, consistent with the observed velocity. These fall into two broad classes (much like models for the TDE luminosity), which have been revealed through detailed TDE simulations. Collisions between debris streams can launch material on unbound trajectories (Jiang et al. 2016b), or drive an outflow via shocks (Lu & Bonnerot 2020). Alternatively, radiatively inefficient accretion can lead to most of the energy from the fallback going into mechanical outflows. Metzger & Stone (2016) described this process analytically, and recent work by Liptai (private communication) has demonstrated that this does occur in first-principles numerical simulations.

Our early observations of AT2019qiz at all wavelengths help to break the degeneracy in these models. The detection of X-rays during this early phase could indicate that accretion began promptly: stream collisions are not predicted to be X-ray sources (Piran et al. 2015), whereas X-ray observations of TDEs to date are generally consistent with disc models (Jonker et al. 2020; Mummery & Balbus 2020; Wevers 2020). The X-rays are not likely to arise from the outflow, as the luminosity is orders of magnitude greater than that predicted by modelling the radio SED (Alexander et al., in preparation). Moreover, we see indications of Bowen fluorescence (N III and likely O III) in the early spectra, and these require a far-UV source to photoionize He II (the Bowen lines are pumped by He II Lyα; Bowen 1935). Leloudas et al. (2019) also interpreted Bowen lines in several TDEs as a signature of obscured accretion.

We also note the UV excess in the light curve at peak, relative to the TDE model that best fits the optical bands (Fig. 12). The UV excess could be explained as a consequence of multiple energy sources contributing to the light curve, i.e. accretion and collisions. In other TDEs, a UV excess has been seen at late times, even in the form of a second maximum in the light curve (Leloudas et al. 2016; Wevers et al. 2019b), with the first peak interpreted as stream collisions and the second as the formation of a disc. If accretion begins sufficiently early, we may see both processes at once, giving a light curve at peak that cannot be easily fit with a one-component model.

7.1.2 *The constant-radius phase*

At the point when its bolometric light curve peaks, AT2019qiz transitions to a rather different behaviour: rapid cooling at constant radius (Fig. 9). In the context of an outflow model, this may be a consequence of the optical depth in the ejecta. Metzger & Stone (2016) argue that the wind is initially optically thick, and that photons are advected outwards to a characteristic trapping radius where they can escape. This advection is responsible for downgrading the X-rays released by accretion to UV/optical photons.

Using our inferred SMBH mass and impact factor in equation (24) from Metzger & Stone (2016), we estimate a trapping radius for AT2019qiz of $\sim 2 \times 10^{14}$ cm, within a factor of a few of our measured photospheric radius at maximum light. Therefore we suggest that the photosphere follows the debris outwards, unable to cool efficiently until the expansion reaches this trapping radius, at which point photons can free-stream from the outer ejecta and the effective photosphere stays frozen, despite continued expansion of the outflow.

The matter at the photosphere is now able to cool. From photon diffusion (Metzger & Stone 2016), this occurs on a time-scale

$$t_{cool} \sim \tau_{es} R_{ej}/c \approx 3\kappa_{es} M_{ej}/4\pi Rc, \quad (1)$$

which is ∼10 d if we assume $R \sim R_{ph} = 6 \times 10^{14}$ cm, with an ejected mass $M_{ej} \sim 0.1\,M_\odot$ above the photosphere and an electron scattering opacity $\kappa_{es} = 0.34\,cm^2\,g^{-1}$ for hydrogen-rich matter. This is reasonably well matched to the duration of this phase of the evolution.

During this short-lived phase, the line profiles change dramatically: by around 20 d after maximum light, the He II profile is roughly symmetrical and shows no evidence of a net velocity offset. We interpret this as supporting evidence for a model where the expansion and eventual cooling of the outflow lead to a reduction in the optical depth, and hence the disappearance of the broadened, blueshifted profiles visible during the rising phase.

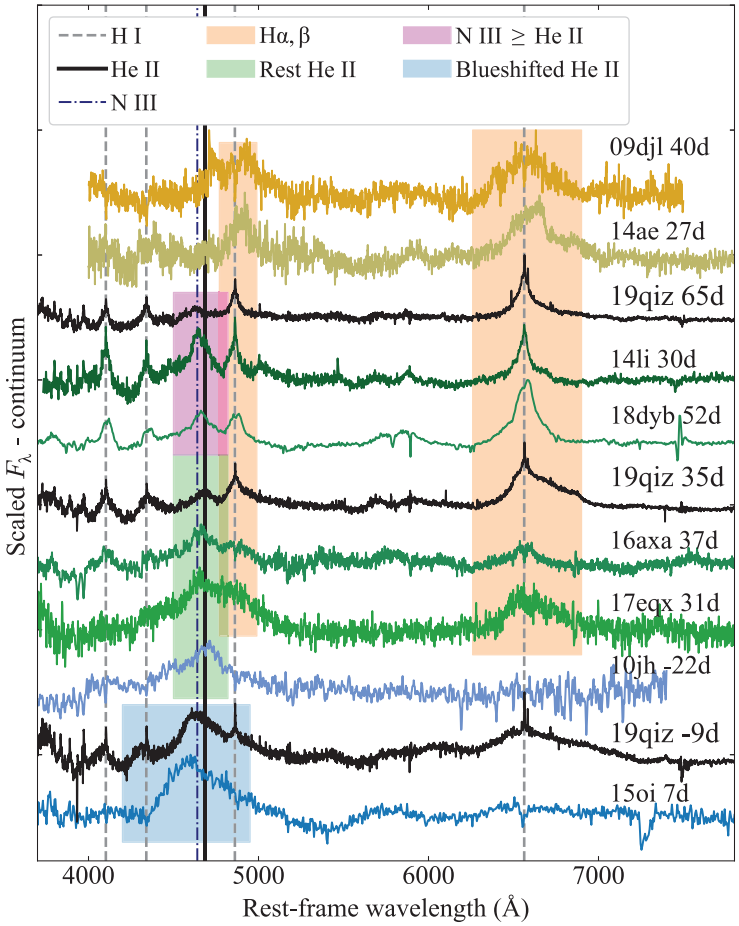

Figure 20. AT2019qiz in the context of the H-Bowen-He sequence of TDE spectra (Arcavi et al. 2014; Leloudas et al. 2019; Nicholl et al. 2019b; van Velzen et al. 2020). Although this TDE is best classified as Bowen type, at various phases the line profile in the Bowen/He region of the spectrum most closely resembles events with blueshifted He II (e.g. ASASSN-15oi; Holoien et al. 2016b), rest-frame He II (e.g. iPTF16axa; Hung et al. 2017), or strong N III (e.g. AT2018dyb, ASASSN-14li; Holoien et al. 2014; Leloudas et al. 2019). The Balmer line profiles are most similar to these latter events.

7.1.3 The constant-temperature phase

At the point when the blueshifts vanish from the line profiles, the behaviour of the photosphere changes again: the cooling stops, the temperature settling at ≈15 000 K, and the radius now begins a smooth decrease. This is more akin to the typical behaviour seen in other optical TDEs, which generally show constant temperatures and decreasing blackbody radii.

At the same time, we observe a rise in the X-ray light curve (Fig. 5), indicating that as the luminosity emitted from the outflowing photosphere fades, at this phase we are seeing more directly the contribution of accretion. The X-ray/optical ratio increases, but remains low ($\lesssim 10^{-2}$; Fig. 9), meaning that most of the accretion power is still reprocessed by the optically thick inner part of the outflow acting as the Eddington envelope (Loeb & Ulmer 1997). The spectral evolution confirms this, as the presence of strong Bowen lines requires the absorption of significant far-UV/X-ray flux by the ejecta.

The X-ray and optical luminosity both decline from here, consistent with a decreasing accretion rate, as also inferred from the MOSFIT model fit. As the accretion power decreases, so too will the energy injected into the mechanical outflow, leading to a decreasing velocity and therefore possibly a higher density (for the same degree of mass loading) in the inner regions. This may explain the increasing prominence of N III at this phase, as the Bowen mechanism is more efficient at high density (Bowen 1935; Netzer et al. 1985). Assuming ∼0.1 $M_\odot$ of hydrogen-dominated debris in the reprocessing region and taking the photospheric radius of ≈3 × 10^{14} cm at this phase, we find an electron density $N_e \approx 10^{12} f_{\rm ion}\,{\rm cm}^{-3}$, where $f_{\rm ion}$ is the ionization fraction, which for even modest ionization is consistent with the density regime, $N_e > 10^{10}\,{\rm cm}^{-3}$, where Bowen lines are expected to be strong (Netzer et al. 1985).

We note however that other TDEs have shown a decreasing N III/He II ratio at late times (Leloudas et al. 2019), which is harder to explain with an increasing density in the reprocessing layer. We posit that this could arise from a viewing angle effect in a geometry similar to that proposed by Nicholl et al. (2019b) to explain the late onset of blueshifted He II in AT2017eqx. If a TDE has a quasi-spherical photosphere but a faster outflow along the polar direction, and is viewed off-axis (see their fig. 13), more low-density material (emitting He II but not N III) will become visible along the dominant axis over time.

The corollary to this picture is that a TDE with an increasing N III/He II ratio (like AT2019qiz) must have been viewed more directly 'face-on'. Such a scenario is supported by the detection of X-rays, which may be visible only for viewing angles close to the pole in the unified model of Dai et al. (2018). In fact, consistency

is also found with Nicholl et al. (2019b), who suggested that TDEs with outflow signatures in their early spectra should also exhibit X-ray emission, since both features are more likely for a polar viewing angle if the outflow is not spherical.

It is interesting to note that the X-rays in AT2019qiz are among the faintest observed in a TDE to date, and would not have been detectable at the greater distances where most TDEs have been found. Deeper X-ray observations of a larger TDE sample are still needed to test for any correlations between the X-ray properties and those of the optical spectral lines. An X-ray to optical ratio that increases with time has been seen in other TDEs (Gezari, Cenko & Arcavi 2017; Wevers et al. 2019b; Jonker et al. 2020), and may be a common feature even for TDEs with a low X-ray luminosity at peak.

7.1.4 Overall energetics

One persistent question pertaining to TDEs is the so-called 'missing energy' problem (Lu & Kumar 2018). This states that the observed luminosity, totalling $\lesssim 10^{51}$ erg for most TDEs, is orders of magnitude below the available energy from the accretion of any significant fraction of a solar mass on to the SMBH. Examining our MOSFIT parameters for AT2019qiz, we have a bound mass of $\approx 0.5\,M_{\odot}$, and a radiative efficiency of ≈ 1 per cent (typical of observed TDEs; Mockler et al. 2019). This gives a total available energy of $\approx 10^{52}$ erg, whereas direct integration of the bolometric light curve yields only 10^{50} erg.

In comparison, a homologously expanding outflow of similar mass with a scale velocity $\sim 10\,000\,\mathrm{km\,s^{-1}}$ carries a total energy of 3×10^{50} erg. This indicates that the fraction of energy going into the mechanical outflow is greater than that released as radiation. However, this is not enough to account for the apparently missing energy. Particularly at early times, accretion can be very inefficient (at producing radiation or driving outflows), and if the infall is spherically symmetric much of the energy can be simply advected across the event horizon.

Lu & Kumar (2018) suggest that most of the energy is radiated promptly in the far-UV. This seems unlikely for AT2019qiz, as the total energy in soft X-rays over the time of our observations is only ~ 1 per cent of the near-UV/optical total, and neither the modest blackbody temperature ($\sim$15 000–20 000 K) nor the shallow power-law in the X-rays (Fig. 4) point towards a large far-UV excess. Still, this scenario can be tested by future searches for a mid-infrared echo on time-scales of $\sim$ years (Jiang et al. 2016a; Lu & Kumar 2018)

Alternatively, a large fraction of the energy can be released in the UV and X-rays not promptly, but rather over $\sim$ decade-long time-scales via ongoing accretion in a stable viscous disc. Indications of such behaviour have been observed for a number of nearby optical TDEs via late-time flattening in the UV light curves (van Velzen et al. 2018) and X-ray observations (Jonker et al. 2020). At our estimated accretion efficiency, AT2019qiz could radiate the rest of its expected total energy ($\sim 10^{52}$ erg) by accreting a few per cent of a solar mass per year. Recently, Wen et al. (2020) modelled the X-ray spectra of TDEs and found that a combination of a 'slimming disc' with a very slowly declining accretion rate, and the energy directly lost into the black hole without radiating, appeared to solve the missing energy problem for the systems they studied. The proximity of AT2019qiz makes it an ideal source to test these scenarios with continued monitoring.

7.2 The nature of faint and fast TDEs

Based on the light-curve comparisons in Section 5, AT2019qiz appears to be the second faintest and fastest among known TDEs. To better quantify this statement, we examine the comprehensive TDE sample from van Velzen et al. (2020), and define a 'faint and fast' TDE as one with a peak blackbody luminosity $\log(L/\mathrm{erg\,s^{-1}}) < 43.5$ and exponential rise time $t_{\rm r} < 15$ d. Four events meet these criteria: AT2019qiz, iPTF16fnl, PTF09axc, and AT2019eve. However, van Velzen et al. (2020) also find that there is no correlation between the rise and decline time-scales of TDEs (unlike SNe; Nicholl et al. 2015). AT2019eve is one of the slowest-fading TDEs, and so appears to be qualitatively different from AT2019qiz and iPTF16fnl, which evolve rapidly in both their rise and decline phases. The remaining event, PTF09axc, has little data available after peak to measure the decline time-scale, but appears to be more symmetrical than AT2019eve.

Of all optical TDEs with host galaxy mass measurements, iPTF16fnl and AT2019eve are among only four with host masses $\log(M_*/M_{\odot}) < 9.5$ (van Velzen et al. 2020), the others being AT2017eqx and AT2018lna, which have more typical light curves (Nicholl et al. 2019b; van Velzen et al. 2020). This suggests that the fastest events may be linked to low-mass SMBHs, as proposed by Blagorodnova et al. (2017). However, the case of AT2019qiz demonstrates that similar events can occur in more massive galaxies, and the SMBH mass we measure, $\sim 10^6\,M_{\odot}$, is typical of known TDEs (Mockler et al. 2019; Wevers et al. 2019a)

We also found that AT2019qiz is similar to iPTF16fnl in its spectroscopic properties at early times (though the strong narrow component in the Balmer lines at later times, possibly associated with an existing BLR, was not observed in iPTF16fnl; Blagorodnova et al. 2017; Onori et al. 2019). Both are classified as TDE-Bowen by van Velzen et al. (2020), and have characteristically small blackbody radii at maximum light. However, the rise and decay time-scales for the TDE-Bowen class as a whole span a similar range to the TDE-H class, so a small radius alone is not sufficient to lead to a fast light curve. Moreover, AT2019eve and PTF09axc are both of type TDE-H.

As the early phase when AT2019qiz and iPTF16fnl are most similar is also the time when the dynamics of the outflow control the light-curve evolution of AT2019qiz, it is possible that the properties of the outflow are most important for causing fast TDEs. In this case, such events may indeed be more common at lower SMBH mass, as the escape velocity from the tidal radius scales as $v_{\rm esc} \propto M_{\bullet}^{1/3}$, meaning an outflow can escape more easily at low $M_{\bullet}$, but are not limited to low-mass black holes as other factors, such as the impact parameter, can also have an effect. Low SMBH mass also lends itself to faint TDEs, if the population have similar Eddington ratios, such that many of these fast TDEs should also be faint. AT2019qiz is only somewhat underluminous, consistent with its more typical SMBH mass.

While iPTF16fnl does show early-time line profiles consistent with an outflow (blueshifted Hα), it was not detected to deep limits in the radio, despite being at a comparable distance to AT2019qiz. While analysis of the radio data for AT2019qiz is deferred to a forthcoming work, we suggest that a pre-existing AGN in this galaxy may lead to a higher ambient density around the SMBH, producing a more luminous radio light curve as the TDE outflow expands into this medium. This is consistent with the overrepresentation of pre-existing AGNs within the sample of radio-detected TDEs (Alexander et al. 2020). Note that the outflows discussed here are not relativistic jets, which could be detectable at any plausible nuclear density (Generozov et al. 2017).

8 CONCLUSIONS

We have presented extensive optical, UV and X-ray observations of AT2019qiz, which is the closest optical TDE to date at only 65.6 Mpc, and a comprehensive analysis of its photometric and spectroscopic evolution. We summarize our main findings here.

(i) AT2019qiz occurred in a galaxy likely hosting a weak AGN, as indicated by BPT line ratios and a nuclear point source. The galaxy has a high central concentration, as seen in other TDE hosts, and a strong quenching of the star formation within the last ∼1 Gyr.

(ii) The SMBH mass, measured using the $M_\bullet - \sigma$ relation, is $10^{5.75}$–$10^{6.52}$ $M_\odot$, depending on the calibration used. The mass inferred from light-curve modelling, $10^{5.9}$ $M_\odot$, is within this interval.

(iii) The bolometric light curve shows a rise in luminosity $L \propto t^2$, consistent with expansion at constant temperature and velocity ≈2200 km s^{-1}.

(iv) The decay is steeper than the canonical $L \propto t^{-5/3}$ but close to the $t^{-8/3}$ predicted for a partial disruption (Ryu et al. 2020). The best-fitting light-curve model with MOSFIT also suggests a partial disruption, of a ≈1 $M_\odot$ star, with about 75 per cent of the star stripped during the encounter.

(v) The peak luminosity, $L = 3.6 \times 10^{43}$ erg s^{-1}, and integrated emission, $E = 1.0 \times 10^{50}$ erg, are both among the lowest measured for a TDE to date.

(vi) The early spectra show broad emission lines of *H* and most likely He II, with blueshifted peaks and asymmetric red wings, consistent with electron scattering in an expanding medium with $v \approx 3000$–$10\,000$ km s^{-1}.

(vii) Around maximum light, the temperature suddenly drops while the radius stays constant. This can be explained as trapped photons advected by the outflow suddenly escaping when it reaches the radius at which the optical depth is below unity.

(viii) After peak, the lines become much more symmetrical, and He II is gradually replaced by N III, indicating efficient Bowen fluorescence and thus a source of far-UV photons. The late-time H lines show an unusually strong peak which may be from a pre-existing BLR.

(ix) The time-varying X-ray emission (i.e. from the TDE rather than the pre-existing AGN) and Bowen lines suggest that accretion commenced early in this event.

The detection of this event at radio wavelengths, likely enabled by its fortuitous proximity and possibly a high ambient density, confirms a (non-relativistic; Alexander et al., in preparation) expansion. This removes ambiguity in interpreting the line profiles of AT2019qiz as arising in an outflow, and confirms the velocities we have inferred from its optical properties. By extrapolation, outflows (even if undetected in the radio in the general case) are likely important in the many other TDEs with similar line profiles to AT2019qiz.

The properties of the outflow in this case (size, density, optical depth) are consistent with the reprocessing layer needed to explain the low X-ray luminosities of most optical TDEs, and in particular to provide the high-density conditions required for Bowen fluorescence in the inner regions. Thus, AT2019qiz offers perhaps the strongest support to date for the long-standing picture that outflows are responsible for the 'Eddington envelope' hypothesized to do this reprocessing (Loeb & Ulmer 1997; Strubbe & Quataert 2009; Guillochon et al. 2014; Metzger & Stone 2016). The evidence for accretion early in this event, including X-ray detections before maximum light, suggest that the outflow was in this case powered by radiatively inefficient accretion (Metzger & Stone 2016; Liptai et al., in preparation), rather than stream collisions.

The exquisite data presented here will make AT2019qiz a Rosetta stone for interpreting future TDE observations in the era of large samples expected from ZTF (van Velzen et al. 2020), the Rubin Observatory (LSST Science Collaboration 2009) and other new and ongoing time-domain surveys.

ACKNOWLEDGEMENTS

We thank the anonymous referee for their many suggestions that improved this paper. We thank Miguel Pérez-Torres for helpful discussions. MN is supported by a Royal Astronomical Society Research Fellowship. TW is funded in part by European Research Council grant 320360 and by European Commission grant 730980. PGJ and GC acknowledge support from European Research Council Consolidator Grant 647208. GL and PC are supported by a research grant (19054) from Villum Fonden. MG is supported by the Polish NCN MAESTRO Grant 2014/14/A/ST9/00121. NI is partially supported by Polish NCN DAINA Grant 2017/27/L/ST9/03221. IA is a CIFAR Azrieli Global Scholar in the Gravity and the Extreme Universe Program and acknowledges support from that program, from the Israel Science Foundation (grant numbers 2108/18 and 2752/19), from the United States-Israel Binational Science Foundation (BSF), and from the Israeli Council for Higher Education Alon Fellowship. JB, DH, and CP were supported by NASA Grant 80NSSC18K0577. TWC acknowledges the EU Funding under Marie Skłodowska-Curie grant agreement No. 842471. LG was funded by the European Union's Horizon 2020 Framework Programme under the Marie Skłodowska-Curie grant agreement No. 839090. This work has been partially supported by the Spanish grant PGC2018-095317-B-C21 within the European Funds for Regional Development (FEDER). SGG acknowledges support by FCT under Projects CRISP PTDC/FIS-AST-31546 and UIDB/00099/2020. IM is a recipient of the Australian Research Council Future Fellowship FT190100574. TMB was funded by the CONICYT PFCHA/DOCTORADOBECAS CHILE/2017-72180113. KDA acknowledges support provided by NASA through the NASA Hubble Fellowship grant *HST*-HF2-51403.001-A awarded by the Space Telescope Science Institute, which is operated by the Association of Universities for Research in Astronomy, Inc., for NASA, under contract NAS5-26555. This work is based on data collected at the European Organisation for Astronomical Research in the Southern Hemisphere, Chile, under ESO programmes 1103.D-0328 and 0104.B-0709 and as part of ePESSTO+(the advanced Public ESO Spectroscopic Survey for Transient Objects Survey), observations from the Las Cumbres Observatory network, the 6.5 meter Magellan Telescopes located at Las Campanas Observatory, Chile, the MMT Observatory, a joint facility of the University of Arizona and the Smithsonian Institution and the William Herschel Telescope (programme W19B/P7). *Swift* data were supplied by the UK Swift Science Data Centre at the University of Leicester. The Liverpool Telescope and William Herschel Telescope are operated on the island of La Palma by Liverpool John Moores University in the Spanish Observatorio del Roque de los Muchachos of the Instituto de Astrofisica de Canarias with financial support from the UK Science and Technology Facilities Council.

DATA AVAILABILITY

All data in this paper will be made publicly available via WISeREP and the Open TDE Catalog.

REFERENCES

Alexander K. D., Berger E., Guillochon J., Zauderer B. A., Williams P. K. G., 2016, ApJ, 819, L25
Alexander K. D., van Velzen S., Horesh A., Zauderer B. A., 2020, Space Sci. Rev., 216, 81
Alexander K. D., Wieringa M. H., Berger E., Saxton R. D., Komossa S., 2017, ApJ, 837, 153
Anderson M. M. et al., 2019, preprint (arXiv:1910.11912)
Arcavi I. et al., 2014, ApJ, 793, 38
Assef R. J. et al., 2013, ApJ, 772, 26
Auchettl K., Guillochon J., Ramirez-Ruiz E., 2017, ApJ, 838, 149
Auchettl K., Hung T., Foley R. J., Stanek K. Z., Kochanek C. S., Mathur S., Shappee B. J., Holoien T. W. S., 2019, Astron. Telegram, 13143, 1
Baldwin J. A., Phillips M. M., Terlevich R., 1981, PASP, 93, 5
Becker A., 2015, HOTPANTS: High Order Transform of PSF ANd Template Subtraction, Astrophysics Source Code Library, record ascl:1504.004
Bellm E. C. et al., 2019, PASP, 131, 018002
Blagorodnova N. et al., 2017, ApJ, 844, 46
Blagorodnova N. et al., 2019, ApJ, 873, 92
Blanchard P. K. et al., 2017, ApJ, 843, 106
Bloom J. S. et al., 2011, Science, 333, 203
Bonnerot C., Lu W., 2020, MNRAS , 495, 1374
Bowen I. S., 1935, ApJ, 81, 1
Breeveld A. A., Landsman W., Holland S. T., Roming P., Kuin N. P. M., Page M. J., 2011, in McEnery J. E., Racusin J. L., Gehrels N., eds, AIP Conf. Proc. Vol. 1358, An Updated Ultraviolet Calibration for the Swift/UVOT, Am. Inst. Phys., New York., p. 373
Brown J. S. et al., 2018, MNRAS, 473, 1130
Brown T. M. et al., 2013, PASP, 125, 1031
Burrows D. N. et al., 2011, Nature, 476, 421
Cappellari M., 2017, MNRAS, 466, 798
Cardelli J. A., Clayton G. C., Mathis J. S., 1989, ApJ, 345, 245
Cenko S. B. et al., 2012, ApJ, 753, 77
Chornock R. et al., 2014, ApJ, 780, 44
Dai L., McKinney J. C., Miller M. C., 2015, ApJ, 812, L39
Dai L., McKinney J. C., Roth N., Ramirez-Ruiz E., Miller M. C., 2018, ApJ, 859, L20
Evans P. A. et al., 2007, A&A, 469, 379
Evans P. A. et al., 2009, MNRAS, 397, 1177
Fabricant D. et al., 2019, PASP, 131, 075004
Fabricius C. et al., 2016, A&A, 595, A3
Flewelling H. A. et al., 2016, preprint (arXiv:1612.05243)
Foreman-Mackey D., Hogg D. W., Lang D., Goodman J., 2013, PASP, 125, 306
Forster F., 2019, Transient Name Server Discovery Report, 2019-1857, 1
French K. D., Arcavi I., Zabludoff A., 2016, ApJ, 818, L21
French K. D., Arcavi I., Zabludoff A. I., Stone N., Hiramatsu D., van Velzen S., McCully C., Jiang N., 2020b, ApJ, 891, 93
French K. D., Wevers T., Law-Smith J., Graur O., Zabludoff A. I., 2020a, Space Sci. Rev., 216, 32
Freudling W., Romaniello M., Bramich D. M., Ballester P., Forchi V., García-Dabló C. E., Moehler S., Neeser M. J., 2013, A&A, 559, A96
Gafton E., Rosswog S., 2019, MNRAS, 487, 4790
Gaia Collaboration, 2018, A&A, 616, A1
Generozov A., Mimica P., Metzger B. D., Stone N. C., Giannios D., Aloy M. A., 2017, MNRAS, 464, 2481
Gezari S., Cenko S. B., Arcavi I., 2017, ApJ, 851, L47
Gezari S. et al., 2012, Nature, 485, 217
Gomez S. et al., 2020, MNRAS, 497, 1925
Goodman J., Weare J., 2010, Commun. Appl. Math. Comput. Sci., 5, 65
Graur O., French K. D., Zahid H. J., Guillochon J., Mandel K. S., Auchettl K., Zabludoff A. I., 2018, ApJ, 853, 39
Guillochon J., Manukian H., Ramirez-Ruiz E., 2014, ApJ, 783, 23
Guillochon J., Nicholl M., Villar V. A., Mockler B., Narayan G., Mandel K. S., Berger E., Williams P. K. G., 2018, ApJS, 236, 6
Guillochon J., Ramirez-Ruiz E., 2013, ApJ, 767, 25
Gültekin K. et al., 2009, ApJ, 698, 198
Heckman T. M., Ptak A., Hornschemeier A., Kauffmann G., 2005, ApJ, 634, 161
Hills J. G., 1975, Nature, 254, 295
Hinkle J. T. et al., 2020, preprint (arXiv:2006.06690)
Hodgkin S. T., Wyrzykowski L., Blagorodnova N., Koposov S., 2013, Phil. Trans. R. Soc. A, 371, 20120239
Holoien T. W.-S. et al., 2014, MNRAS, 445, 3263
Holoien T. W.-S. et al., 2016a, MNRAS, 455, 2918
Holoien T. W.-S. et al., 2016b, MNRAS, 463, 3813
Holoien T. W.-S. et al., 2019a, ApJ, 880, 120
Holoien T. W.-S. et al., 2019b, ApJ, 883, 111
Huber M. et al., 2015, Astron. Telegram, 7153, 1
Hung T. et al., 2017, ApJ, 842, 29
Hung T. et al., 2019, ApJ, 879, 119
Hung T. et al., 2020, preprint (arXiv:2003.09427)
Jiang N., Dou L., Wang T., Yang C., Lyu J., Zhou H., 2016a, ApJ, 828, L14
Jiang Y.-F., Guillochon J., Loeb A., 2016b, ApJ, 830, 125
Jonker P. G., Stone N. C., Generozov A., Velzen S. v., Metzger B., 2020, ApJ, 889, 166
Jorden P. R., 1990, in Crawford D. L., ed., Proc. SPIE Conf. Ser. Vol. 1235, EEV large-format CCD camera on the WHT ISIS spectrograph. SPIE, Bellingham, p. 790
Kankare E. et al., 2017, Nat. Astron., 1, 865
Kewley L. J., Dopita M. A., Sutherland R. S., Heisler C. A., Trevena J., 2001, ApJ, 556, 121
Kochanek C. S., 1994, ApJ, 422, 508
Komossa S., 2002, in Schielicke R. E., ed., Reviews in Modern Astronomy Vol. 15, JENAM 2001: Astronomy with Large Telescopes from Ground and Space. Springer, Berlin, p. 27
Kormendy J., Ho L. C., 2013, ARA&A, 51, 511
Kostrzewa-Rutkowska Z. et al., 2018, MNRAS, 481, 307
Law-Smith J., Ramirez-Ruiz E., Ellison S. L., Foley R. J., 2017, ApJ, 850, 22
Leja J., Johnson B. D., Conroy C., van Dokkum P. G., Byler N., 2017, ApJ, 837, 170
Leloudas G. et al., 2016, Nat. Astron., 1, 0002
Leloudas G. et al., 2019, ApJ, 887, 218
Liu F. K., Zhou Z. Q., Cao R., Ho L. C., Komossa S., 2017, MNRAS, 472, L99
Loeb A., Ulmer A., 1997, ApJ, 489, 573
LSST Science Collaboration, 2009, preprint (arXiv:0912.0201)
Lu W., Bonnerot C., 2020, MNRAS, 492, 686
Lu W., Kumar P., 2018, ApJ, 865, 128
Marino R. A. et al., 2013, A&A, 559, A114
Masci F. J. et al., 2019, PASP, 131, 018003
Mattila S. et al., 2018, Science, 361, 482
McConnell N. J., Ma C.-P., 2013, ApJ, 764, 184
Merritt D., Poon M. Y., 2004, ApJ, 606, 788
Metzger B. D., Stone N. C., 2016, MNRAS, 461, 948
Mockler B., Guillochon J., Ramirez-Ruiz E., 2019, ApJ, 872, 151
Mummery A., Balbus S. A., 2020, MNRAS, 492, 5655
Netzer H., Elitzur M., Ferland G. J., 1985, ApJ, 299, 752
Nicholl M., 2018, Res. Notes Am. Astron. Soc., 2, 230
Nicholl M., Short P., Lawrence A., Ross N., Smartt S., 2019a, Transient Name Server AstroNote, 59, 1
Nicholl M. et al., 2015, MNRAS, 452, 3869
Nicholl M. et al., 2019b, MNRAS, 488, 1878
Oke J. B. et al., 1995, PASP, 107, 375
Onori F. et al., 2019, MNRAS, 489, 1463
Osterbrock D. E., Ferland G. J., 2006, Astrophysics of Gaseous Nebulae and Active Galactic Nuclei, University Science Books, Sausalito, CA, USA
O'Brien A., Kaplan D., Murphy T., Yu W., Zhang W., 2019, Astron. Telegram, 13334, 1
Patterson M. T. et al., 2019, PASP, 131, 018001
Peng C. Y., Ho L. C., Impey C. D., Rix H.-W., 2002, AJ, 124, 266
Pettini M., Pagel B. E. J., 2004, MNRAS, 348, L59
Phinney E. S., 1989, Proc. 136th IAU Symp., 136, 543
Piascik A. S., Steele I. A., Bates S. D., Mottram C. J., Smith R. J., Barnsley R. M., Bolton B., 2014, in Ramsay S. K., McLean I. S., Takami H., eds,

Proc. SPIE Conf. Ser. Vol. 9147, SPRAT: Spectrograph for the Rapid Acquisition of Transients. SPIE, Bellingham, p. 91478H
Piran T., Svirski G., Krolik J., Cheng R. M., Shiokawa H., 2015, ApJ, 806, 164
Poznanski D., Prochaska J. X., Bloom J. S., 2012, MNRAS, 426, 1465
Prieto J. L. et al., 2016, ApJ, 830, L32
Rees M. J., 1988, Nature, 333, 523
Roth N., Kasen D., 2018, ApJ, 855, 54
Roth N., Kasen D., Guillochon J., Ramirez-Ruiz E., 2016, ApJ, 827, 3
Ryu T., Krolik J., Piran T., Noble S. C., 2020, preprint (arXiv:2001.03503)
Schlafly E. F., Finkbeiner D. P., 2011, ApJ, 737, 103
Shiokawa H., Krolik J. H., Cheng R. M., Piran T., Noble S. C., 2015, ApJ, 804, 85
Shore S. N., Kuin N. P., Mason E., De Gennaro Aquino I., 2018, A&A, 619, A104
Short P. et al., 2020, MNRAS, 498, 4119
Siebert M. R., Strasburger E., Rojas-Bravo C., Foley R. J., 2019, Astron. Telegram, 13131, 1
Skrutskie M. F. et al., 2006, AJ, 131, 1163
Smartt S. J. et al., 2015, A&A, 579, A40
Smith K. W. et al., 2019, Res. Notes Am. Astron. Soc., 3, 26
Smith N., Chornock R., Silverman J. M., Filippenko A. V., Foley R. J., 2010, ApJ, 709, 856
Stern D. et al., 2012, ApJ, 753, 30
Strubbe L. E., Quataert E., 2009, MNRAS, 400, 2070
Tonry J. L. et al., 2018, PASP, 130, 064505
van Dokkum P. G., Bloom J., Tewes M., 2012, L.A. Cosmic: Laplacian Cosmic Ray Identification, recordascl:1207.005
van Velzen S., 2018, ApJ, 852, 72
van Velzen S., Stone N. C., Metzger B. D., Gezari S., Brown T. M., Fruchter A. S., 2019, ApJ, 878, 82
van Velzen S. et al., 2016, Science, 351, 62
van Velzen S. et al., 2019, ApJ, 872, 198
van Velzen S. et al., 2020, preprint (arXiv:2001.01409)
Vernet J. et al., 2011, A&A, 536, A105
Wen S., Jonker P. G., Stone N. C., Zabludoff A. I., Psaltis D., 2020, ApJ, 897, 80
Wevers T., 2020, MNRAS, 497, L1
Wevers T., van Velzen S., Jonker P. G., Stone N. C., Hung T., Onori F., Gezari S., Blagorodnova N., 2017, MNRAS, 471, 1694
Wevers T. et al., 2019a, MNRAS, 487, 4136
Wevers T. et al., 2019b, MNRAS, 488, 4816
Wright E. L. et al., 2010, AJ, 140, 1868
Yaron O., Gal-Yam A., 2012, PASP, 124, 668
Zauderer B. A. et al., 2011, Nature, 476, 425
Zhang W., Yu W., Yan Z., Rapisarda S., 2019, Astron. Telegram, 13146, 1

APPENDIX A: HOST GALAXY SUBTRACTION

A1 UV photometry

Fig. A1 shows the difference between the host-subtracted UVOT light curves using a 5 arcsec aperture compared to a 30 arcsec aperture, as described in Section 3.3.

A2 Spectroscopy

The PROSPECTOR model spectrum allows us to remove stellar continuum from our spectroscopic data to better study emission from the TDE. Fig. A2 illustrates the method. We first construct an *r*-band light curve measured from LCO data (without any image subtraction) in an aperture of radius 3 arcsec, chosen to match the typical aperture size used for extracting the spectrum. This unsubtracted light-curve

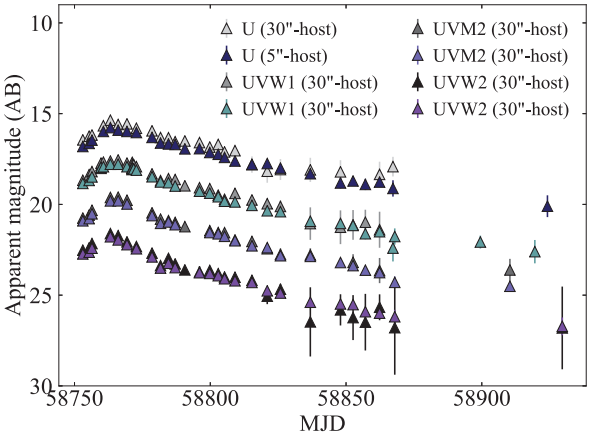

Figure A1. Host subtraction from UVOT magnitudes. The grey points show photometry measured in a large 30 arcsec aperture to fully capture the transient and host flux, with the entire host flux from the PROSPECTOR model in each band subtracted. The coloured triangles show the UVOT photometry measure in a 5 arcsec aperture, where the calibration is more reliable and the host contamination lower, with 10–20 per cent of the total host flux subtracted.

plateaus when the TDE light falls below that of the host. We then scale each spectrum (remembering that it also contains both host and TDE light) to match this light curve; synthetic photometry is calculated on the spectrum using PYSYNPHOT.

The model host spectrum from PROSPECTOR is scaled to $m_r = 16.47$ mag, measured in a matching 3 arcsec aperture in the PanSTARRS *r*-band image. At each epoch, this model spectrum is interpolated to the same wavelength grid as the data, convolved with a Gaussian function to match the instrument-specific resolution, and subtracted. We verify that the fraction of flux removed in this way is reasonable by performing synthetic photometry on the subtracted spectrum, and find that it matches the *host-subtracted* photometry to better than 0.5 mag at all times. As a final step, we apply a small scaling to the subtracted spectrum to correct these $\lesssim$ few $\times$ 0.1 mag discrepancies with the subtracted light curve.

Fig. A2 also shows the spectrum of AT2019qiz at 125 d after the light-curve peak (i.e. when host light is the dominant component) compared to the host model, after scaling to the observed magnitudes and convolving to match the resolution, as described above. The middle panel shows the full optical range, showing the good match to the continuum shape, with some TDE emission lines clearly visible above the host level. The host model shows deep Balmer absorption lines (common in TDE host galaxies) while the subtraction residuals (i.e. the TDE-only spectrum, also plotted) exhibits prominent Balmer emission. To verify that these are real features rather than oversubtraction, we show close-ups around several of the main host absorption lines. The model gives an excellent match to the Ca II, Mg I, Na I, and *G*-band absorptions present in the data, giving us confidence that the TDE H emission is real (and cancels out the host absorptions in the bluer Balmer lines). Moreover, the TDE shows a clear H α (and weak H β) emission line even before subtraction, with a profile similar to the emission lines in the subtracted spectrum. Finally, we find that the emission-line fluxes decrease with time, which would not be true in the case of oversubtraction

Fig. A3 shows all spectra of AT2019qiz as in Fig. 6, but in this case after applying the host subtraction process.

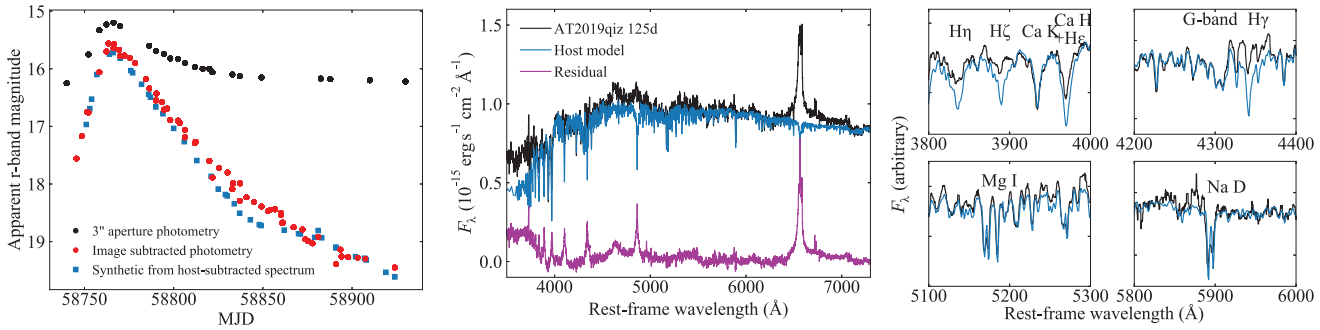

Figure A2. Removing host galaxy light from the TDE spectra. Left: raw aperture photometry in the central 3 arcsec (includes host emission) versus image-subtracted PSF-fitting photometry (no host). Each TDE spectrum is scaled to the former (interpolated to epochs with spectra) before subtraction, and the synthetic magnitude after subtracting the host is verified to closely match the latter. Middle: a late-time spectrum of AT2019qiz compared to the host model, which has been scaled and convolved to match the data. Subtraction residuals (i.e. the TDE-only spectrum) are also shown. Right: close-ups of strongest host galaxy absorption lines. We obtain an excellent match between the observed and PROSPECTOR-predicted equivalent widths of the metal lines. The model predicts Balmer absorptions that are not observed in the data due to filling by the TDE emission lines.

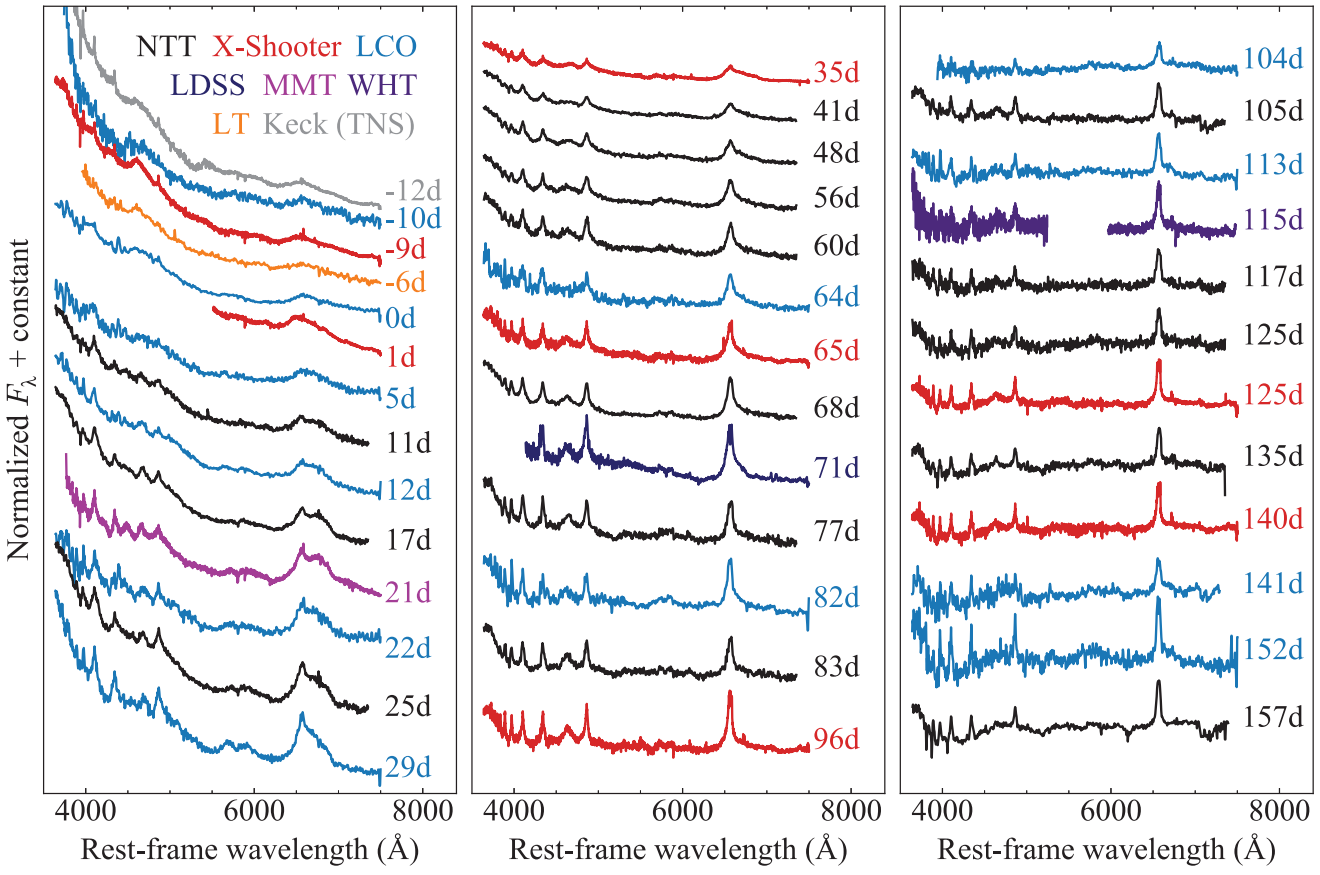

Figure A3. Same as Fig. 6 but with host contribution removed.

APPENDIX B: MOSFIT POSTERIORS

The priors and marginalized posteriors of our MOSFIT TDE model were listed in Table 2. In Fig. B1, we plot the full two-dimensional posteriors, which show some degeneracies between ϵ and β, and $l_{\rm ph}$ and $R_{\rm ph,\,0}$.

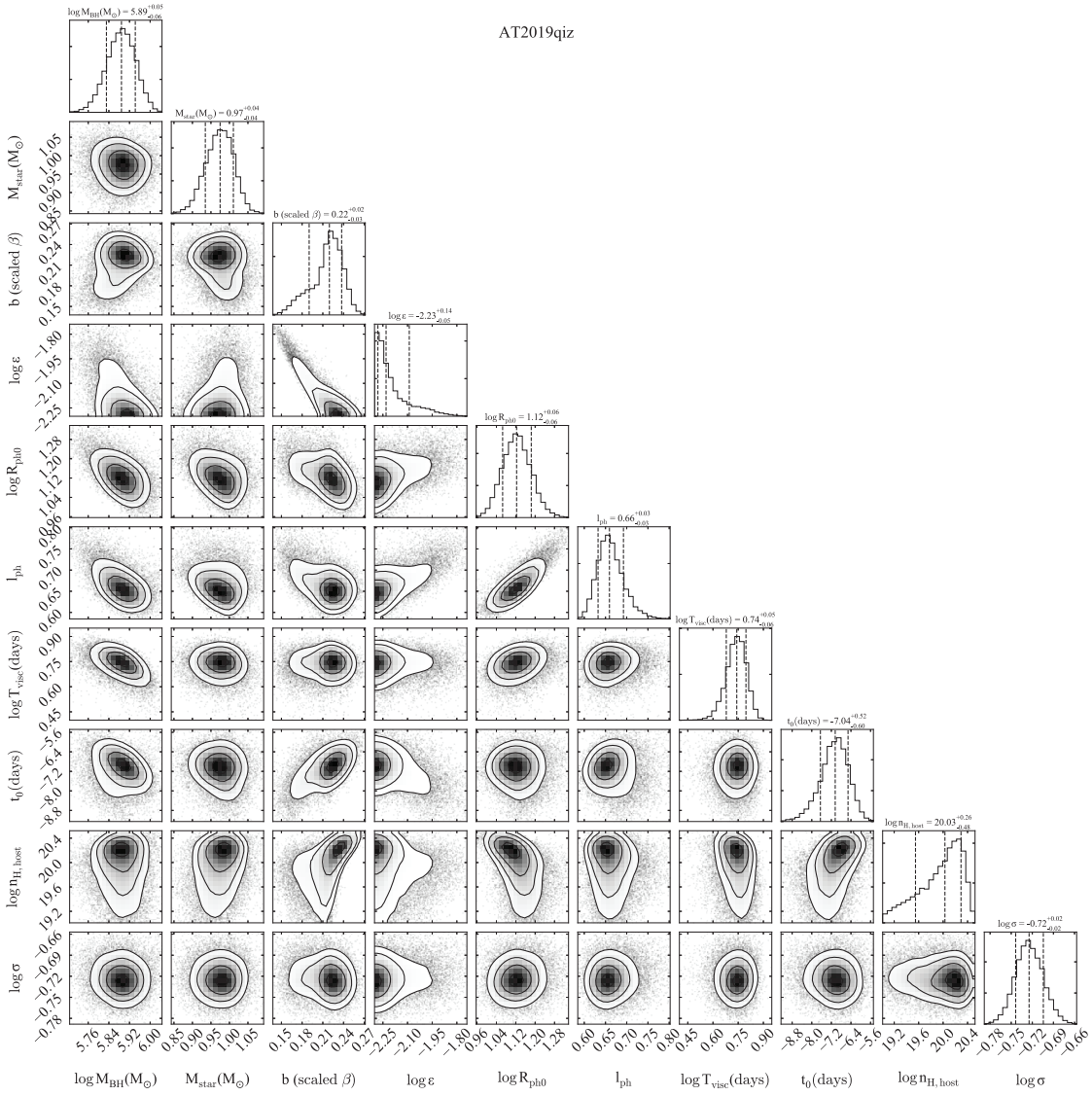

Figure B1. Posterior probability density functions for the free parameters of the model light curves in Fig. 12.

[1]*Birmingham Institute for Gravitational Wave Astronomy and School of Physics and Astronomy, University of Birmingham, Birmingham B15 2TT, UK*
[2]*Institute for Astronomy, University of Edinburgh, Royal Observatory, Blackford Hill EH9 3HJ, UK*
[3]*Institute of Astronomy, University of Cambridge, Madingley Road, Cambridge CB3 0HA, UK*
[4]*Center for Interdisciplinary Exploration and Research in Astrophysics and Department of Physics and Astronomy, Northwestern University, 2145 Sheridan Road, Evanston, IL 60208-3112, USA*
[5]*DTU Space, National Space Institute, Technical University of Denmark, Elektrovej 327, DK-2800 Kgs. Lyngby, Denmark*
[6]*Istituto di Astrofisica e Planetologia Spaziali (INAF), Via Fosso del Cavaliere 100, I-00133 Roma, Italy*
[7]*Max-Planck-Institut für Astrophysik, Karl-Schwarzschild Str. 1, D-85748 Garching, Germany*
[8]*Department of Astronomy, Stockholm University, The Oskar Klein Centre, AlbaNova, SE-106 91 Stockholm, Sweden*
[9]*Center for Astrophysics | Harvard & Smithsonian, 60 Garden Street, Cambridge, MA 02138-1516, USA*
[10]*INAF-Osservatorio Astronomico di Brera, via Bianchi 46, I-23807 Merate (LC), Italy*
[11]*The School of Physics and Astronomy, Tel Aviv University, Tel Aviv 69978, Israel*
[12]*CIFAR Azrieli Global Scholars program, CIFAR, 661 University Ave. Suite 505, Toronto, ON M5G 1M1, Canada*
[13]*Astronomical Observatory, University of Warsaw, Al. Ujazdowskie 4, PL-00-478 Warszawa, Poland*
[14]*Department of Astrophysics/IMAPP, Radboud University, PO Box 9010, NL-6500 GL Nijmegen, the Netherlands*
[15]*SRON, Netherlands Institute for Space Research, Sorbonnelaan 2, NL-3584 CA Utrecht, the Netherlands*
[16]*Monash Centre for Astrophysics, School of Physics and Astronomy, Monash University, Clayton, Victoria 3800, Australia*
[17]*The ARC Center of Excellence for Gravitational Wave Discovery–OzGrav, Swinburne University of Technology, PO Box 218, Hawthorn, VIC 3122, Australia*
[18]*Department of Particle Physics and Astrophysics, Weizmann Institute of Science, 234 Herzl St, Rehovot 76100, Israel*
[19]*Las Cumbres Observatory, 6740 Cortona Dr, Suite 102, Goleta, CA 93117-5575, USA*

[20]*Department of Physics, University of California, Santa Barbara, CA 93106-9530, USA*
[21]*The Research School of Astronomy and Astrophysics, Australian National University, Canberra, ACT 2601, Australia*
[22]*European Southern Observatory, Alonso de Cońdova 3107, Vitacura, Casilla 190001, Santiago, Chile*
[23]*Institute of Astrophysics Paris (IAP), and Sorbonne University, 98bis Boulevard Arago, F-75014 Paris, France*
[24]*Departamento de Física Teórica y del Cosmos, Universidad de Granada, E-18071 Granada, Spain*
[25]*CENTRA-Centro de Astrofísica e Gravitação and Departamento de Física, Instituto Superior Técnico, Universidade de Lisboa, Avenida Rovisco Pais, P-1049-001 Lisboa, Portugal*
[26]*School of Physics & Astronomy, Cardiff University, Queens Buildings, The Parade, Cardiff CF24 3AA, UK*
[27]*Mullard Space Science Laboratory, University College London, Holmbury St Mary, Dorking, Surrey RH5 6NT, UK*
[28]*School of Physics and Astronomy, University of Southampton, Southampton SO17 1BJ, UK*
[29]*Departamento de Ciencias Fisicas, Universidad Andrés Bello, Avda. Republica 252, Santiago, Chile*
[30]*The Inter-University Centre for Astronomy and Astrophysics, Ganeshkhind, Pune 411007, India*
[31]*Astrophysics Research Centre, School of Mathematics and Physics, Queens University Belfast, Belfast BT7 1NN, UK*

This paper has been typeset from a TEX/LATEX file prepared by the author.